

https://dspace.org/

H.E.S.S. observations of the Gamma-ray Binary LMC P3

Fisher, Lalenthra

2024
https://hdl.handle.net/10539/37435

Downloaded from a DSpace repository. https://dspace.org/

H.E.S.S. Observations of the Gamma-ray Binary LMC P3

Lalenthra Fisher
1599588

Supervisor:
Prof. Dr. Nukri Komin



A dissertation submitted in fulfilment of the requirements for the degree of

Master of Science

in

Physics

in the Faculty of Science, University of the Witwatersrand, Johannesburg

14 June 2023

Declaration

I, Lalenthra Fisher, declare this dissertation is my own, unaided work. It is being submitted for the degree of Master of Science at the University of the Witwatersrand, Johannesburg. It has not been submitted for any degree or examination at any other university.



Lalenthra Fisher

14 June 2023

"The amount of it, be sure, is merely a Scream, but sometimes a scream is better than a thesis."

Ralph Waldo Emerson

Abstract

Context: The first extra-galactic gamma-ray binary, LMC P3, is a gamma-ray binary comprising of an unconfirmed compact object and an O-star and is located in the Large Magellanic Cloud. Initially discovered in Fermi-LAT data, it shows an orbital period of 10.3 days. H.E.S.S. has reported the detected Very High Energy (VHE) gamma-ray emission during only 20% of the orbit (Abdalla et al. 2018), between orbital phases 0.2 and 0.4, which roughly corresponds to the inferior conjunction of the compact object.

Purpose: H.E.S.S. has continued the observations of this object since then. This work aims to produce a data analysis with a much deeper data set. The new data allowed for a more precise measurement of the location of the VHE gamma-ray peak along the orbit of the system to be made.

Methods: Using LMC observations from the HESS array from 2003-2022, a spectral and temporal analysis was conducted using the analysis package *Gammapy*. N 157B is used as a standard candle for a consistency check. The analysis incorporates the latest orbital solutions for the system.

Results: The peak of the VHE emission was found at a phase 0.268 - 0.366, which with the current orbital solution, places this after inferior conjunction.

Conclusions: The VHE light curve is better constrained w.r.t. the previous H.E.S.S. publication(Abdalla et al. 2018). The peak of emission is reduced from 20% to just under 10% of the orbital period. In-depth physical modelling is required to explain the physical origin of the VHE gamma-ray emission.

Acknowledgements

I want to acknowledge my supervisor, Nukri Komin, who offered exceptional guidance and mentorship throughout my university career, especially in my post-graduate research. I also thank the Wits Centre for Astrophysics (Wits CfA) for access to the remote server.

This work is based on the research supported in part by the National Research Foundation of South Africa (Grant number: MND210616612142). I acknowledge that opinions, findings and conclusions or recommendations expressed in any publication generated by the NRF-supported research are that of mine alone, and that the NRF accepts no liability whatsoever in this regard.

Contents

Declaration i

Abstract iii

Acknowledgements iv

List of Figures ix

List of Tables xi

List of Abbreviations xii

1 Introduction 1
- 1.1 Background . . . 1
  - 1.1.1 Very High Energy (VHE) Gamma-ray Astronomy . . . 1
  - 1.1.2 VHE Gamma-ray Emission from Binary Systems . . . 2
- 1.2 Problem Statement . . . 3
- 1.3 Research Question . . . 4
- 1.4 Research Aims and Objectives . . . 5
  - 1.4.1 Research Aim . . . 5
  - 1.4.2 Objectives . . . 5
- 1.5 Limitations . . . 6
  - 1.5.1 Sensitivity . . . 6
  - 1.5.2 Physical Modelling . . . 6
- 1.6 Outline . . . 6

2 Literature Review 8
- 2.1 Scenarios for Emission . . . 8
  - 2.1.1 Microquasar Scenario . . . 9

2.1.2 Pulsar Wind Scenario . . . 10
2.2 The Compact Object . . . 10
2.2.1 Indirect Evidence for the Pulsar wind Scenario . . . 10
2.2.2 Gamma-ray Binaries vs X-ray binaries . . . 12
Gamma-ray binaries: A Proposed Definition . . . 12
X-ray binaries . . . 13
Commonalities in Accretion and Pulsar Wind Driven Systems 13
Differences in Accretion and Pulsar Wind Driven Systems . . 14
2.3 LMC P3: The Extra-galactic Gamma-ray Binary . . . 15
2.3.1 The LMC Neighbourhood . . . 15
2.3.2 LMC P3 as an X-ray source . . . 15
2.3.3 Gamma-ray detections from LMC P3 . . . 15
2.3.4 Broadband emission . . . 16
2.4 Relativistic Electrons' VHE Gamma-ray Production and Absorption 16
2.4.1 Inverse Compton Scattering . . . 19
2.4.2 Photon-photon Pair Production/Gamma-gamma Absorption 22

3 Research Methodology 25
3.1 Ground-based Gamma-ray Detection . . . 25
3.1.1 Electromagnetic Air Shower . . . 25
Pair Production and Bremsstrahlung . . . 25
Hadronic Air Showers . . . 27
3.1.2 Cherenkov Radiation . . . 27
3.1.3 The H.E.S.S. Experiment . . . 27
The detectors . . . 30
Gamma-ray Selection . . . 30
3.2 Data . . . 31
3.2.1 Observations of the Large Magellanic Cloud . . . 31
Pre-processing/Treatment of data . . . 31
3.3 Methods . . . 32
3.3.1 Software Packages . . . 32
3.3.2 LMC Objects . . . 32
N 157B Spectrum . . . 33
LMC P3 Spectrum . . . 33

LMC P3 Orbital Parameters . . . 33
3.3.3 Run Selection . . . 34
3.4 Analysis: Spectrum . . . 36
3.4.1 Data reduction . . . 36
3.4.2 Spectral Fitting and Flux Estimation . . . 39
3.5 Analysis: Sky Maps . . . 39
3.6 Analysis: Orbital Parameters . . . 39
3.6.1 Orbit Class . . . 39
Phase and True Anomaly calculation . . . 39
3.6.2 Orbital binning . . . 40
3.6.3 Run Sorting . . . 40
3.6.4 Naima Modelling . . . 41
Electron Spectrum . . . 41
Seed Photon Field . . . 42
Model . . . 42

4 Results **43**
4.1 Sky Maps . . . 43
All Runs . . . 43
4.1.1 Orbitally resolved Sky Maps . . . 46
4.2 Spectral Results . . . 50
4.2.1 Background Determination . . . 50
4.2.2 N 157B Consistency Check . . . 51
Data . . . 51
Log Parabola Parameters . . . 51
Flux Estimates . . . 54
4.2.3 LMC P3 . . . 57
Data . . . 57
Power Law parameters . . . 58
Flux Estimates . . . 61
4.2.4 Orbital Binning . . . 62
Phase-resolved Energy Spectrum . . . 62
4.2.5 Light Curve . . . 64
4.3 Naima Modelling . . . 65

5 Discussion **67**
5.1 Research Aims and Objectives 67
5.2 Key Findings 67
5.3 Consistency Check 68
5.3.1 Spectral Analysis: N 157B 68
5.3.2 Testing for constant flux 68
5.4 Sky Maps 69
5.5 Spectral Analysis: LMC P3 69
5.6 Temporal Analysis 69
5.6.1 Light Curve 69
5.7 Implications for gamma-ray emission 70
Naima Modelling 71
Comparisons With other models 71
5.8 Alternative solutions 72
5.9 Limitations and Recommendations 73

6 Conclusion **74**
6.1 Main Contributions 74
6.1.1 Implications 74
6.2 Limitations 75
6.3 Recommendations 75
6.3.1 Further Research 76

List of Figures

2.1 Scenarios for Emission . . . 9
2.2 Broadband Light Curves . . . 17
2.3 VHE Light Curve . . . 18
2.4 Relationship of electron and incoming photon to IC scattered photon 21

3.1 Pair Production in Matter . . . 26
3.2 Bremsstrahlung in Matter . . . 26
3.3 Particle Showers . . . 28
3.4 Cherenkov Radiation opening angle . . . 29
3.5 The binary orientation of LMC P3 showing the star (blue circle), positions of inferior and superior conjunction marked with a + and periastron ×. Source: van Soelen et al. (2019) . . . 35
3.6 Plot of the cumulative excess of the full dataset of LMC P3 plotted over the livetime. . . . 37
3.7 Plot of the cumulative significance of the full dataset of LMC P3 plotted over the livetime. . . . 38
3.8 The true anomaly is the angle, TA, drawn from periastron, through the star and to the current position of the orbiting body, CO. . . . 40
3.9 Orbital binning . . . 41

4.1 Significance Map of the LMC . . . 44
4.2 LMC P3 sky map . . . 45
4.3 Gaussian fit of the off-regions . . . 46
4.4 Significance maps at different orbital phases . . . 48
4.5 Significance maps at different orbital phases . . . 49
4.6 Background determination of LMC P3 . . . 50
4.7 N 157B log parabola fits for various H.E.S.S. configurations . . . 53
4.8 N 157B Spectral Fit . . . 54

4.9 N 157B Log-parabola Spectrum 55
4.10 N157B Light Curve 56
4.11 Significance evolution for LMC P3. 58
4.12 Orbital averaged power law energy spectrum for LMC P3. 59
4.13 On-peak power law energy spectrum for LMC P3. 61
4.14 Power law energy spectrum for LMC P3 at different points in the orbit. 63
4.15 Lightcurve for LMC P3. 65
4.16 Inverse Compton Scattering Model for LMC P3 66

List of Tables

2.1 Differences between HMXB and HMGB 14

3.1 H.E.S.S. analysis configuration modes. 32
3.2 Fixed position of point-like sources in the LMC in Galactic coordinates. The positions of these sources were used to define exclusion regions for background estimation. 33
3.3 Statistical results and spectral parameters for different orbital phase bins of H.E.S.S. J0536-675. The on-peak region covers orbital phases from 0.2 to 0.4, and the off-peak region the orbital phases from 0.4 to 0.2. Orbital phase 0 is defined at the maximum Fermi-LAT emission at MJD 57410.25. Source: Abdalla et al. (2018) 34

4.1 Fit results of the Gaussian off-regions at different orbital phases. . . . 47
4.2 Log Parabola Parameters for N157B. 52
4.3 Data sets for LMC P3. 57
4.4 Power law Parameters for LMC P3. 59
4.5 All runs SED points 60
4.6 Flux estimates for LMC P3. 62
4.7 Pre-inferior SED points 63
4.8 Inferior Conjunction SED points 63
4.9 Post-inferior SED points 64

List of Abbreviations

TeV	Tera-electron volt
GeV	Giga-electron volt
H.E.S.S.	High Energy Stereoscopic System
LMC	Large Magellanic Cloud
VHE	Very High Energy, > 100 GeV
HE	High Energy, 0.1 - 100 GeV
HMXB	High Mass X-ray Binary
PWN	Pulsar Wind Nebula
HESS	High Energy Stereoscopic System
MJD	Modified Julian Date
SED	Spectral Energy Distribution
TA	True Anomaly

To a loving mother, who single-handedly raised three stubborn individuals who will not stop pursuing their dreams, no matter how out of this world.

Chapter 1

Introduction

Since Victor Francis Hess' seminal balloon flights in 1911 and 1912 firmly concluded that the ionising radiation in the upper atmosphere is of cosmic origin (Cirkel-Bartelt 2008), physicists have been invested in studying the processes and sites that can produce these cosmic rays. *Gamma-ray astronomy* is an ideal discipline employed to study the sites and mechanisms of particle acceleration. A system which is a potential cosmic ray production site and the subject of this study is LMC P3, a gamma-ray binary found in the third Fermi-LAT survey (Corbet et al. 2016). This research aims to study this system in the Very High Energy gamma-ray regime.

1.1 Background

This section intends to give the reader a broad overview and motivation of very high energy (VHE, >100 GeV) gamma-ray astronomy as a discipline for studying high-energy non-thermal astrophysical processes and how this pertains to gamma-ray binary systems. The topics and terms introduced here will be expanded upon in later chapters.

1.1.1 Very High Energy (VHE) Gamma-ray Astronomy

The first thing that makes VHE gamma-ray astronomy a valuable discipline for studying non-thermal relativistic processes in astrophysics is that particle acceleration produces gamma rays in copious amounts (Aharonian 2004). VHE gamma-rays can be produces in hadronic interactions, such as π^0-decay, where relativistic protons and nuclei produce gamma rays in inelastic collisions with ambient gas due to the production and decay of secondary pions, kaons and hyperons. Gamma

rays are also produced in leptonic interactions, for instance, one process dominant in TeV gamma rays' production in binary systems is Inverse Compton (IC) Scattering, where relativistic electrons and positrons (the products of particle acceleration) up-scatter ambient photons to TeV energies. Inverse Compton Scattering will be described in chapter 2.
Gamma rays are also not deflected in interstellar and intergalactic magnetic fields since they do not carry a charge, which makes them ideal for being the indirect messengers of cosmic ray studies.

Finally, ground-based instruments effectively detect VHE gamma rays (Aharonian 2004). These instruments, called Imaging Atmospheric Cherenkov Telescopes (IACTs), detected the short bursts of (primarily optical) radiation emitted by electromagnetic cascades when the VHE gamma rays interact with the atmosphere.

1.1.2 VHE Gamma-ray Emission from Binary Systems

The stellar binary systems of interest in High Energy Astrophysics are systems in which one of the two stars have gone supernova and left behind a compact remnant. In the case of a black hole remnant or a white dwarf, accretion of stellar material from the main sequence star can provide the ideal environment for particle acceleration and gamma-ray production. In the case of a pulsar with a suitable spin-down power, relativistic pulsar wind may interact with stellar outflows, creating a similar high-energy environment capable of extreme particle acceleration.
The first prediction of TeV emission from a binary system comes from Kirk et al. (1999), wherein they show that the system PSR B1259-63 (or LS2833) should be able to produce a flux of TeV gamma-rays that can be detected from the current generation of Cherenkov detectors. The system involves a Oe star and a radio pulsar. The H.E.S.S. collaboration subsequently detected VHE gamma rays in 2004 (Aharonian et al. 2005a).

The advent of the current generation of observatories like H.E.S.S. have enabled the discovery of high energy and very high energy gamma rays from binary systems. Gamma-ray binaries emerged as a new source class, a subset of high-mass X-ray binaries with their peak energy output in gamma rays (Dubus 2013). The number of

this source class has steadily increased to around nine (Chernyakova & Malyshev 2020), one of which being LMC P3, the first extra-galactic gamma-ray binary. These systems exhibit modulated TeV emission thought to arise from the interaction between the stellar companion and the compact object.

While modulated TeV emission has been observed from LMC P3 by the H.E.S.S. array in 2018 (Abdalla et al. 2018), the reported light curve consisted of only one statistically significant flux point, which represented 20% of the orbital period, and the rest of the light curve consisted of upper limits. Since this initial publication, H.E.S.S. has done more observations of the LMC and this binary, potentially allowing the resolution of LMC P3's light curve. In addition, van Soelen et al. (2019) have published an orbital solution for the system, allowing for physical modelling of the radiation processes in the system.

This research will use the larger H.E.S.S. dataset and the orbital parameters to construct a resolved light curve and compare the predictions of the physical model with the observed model to see if the model holds up against the observed light curve.

1.2 Problem Statement

LMC P3 has been established as a VHE gamma-ray emitter through observations using H.E.S.S. (Abdalla et al. 2018), demonstrating that the Fermi-LAT and H.E.S.S. light curves are in anti-phase. This is indicative that there are additional factors modulating the TeV emission that does not affect the GeV emission to the same extent. To understand what physical processes are at play in the system, we need to know the system's orbit, obtained in van Soelen et al. (2019).

However, the issue arising from these established works is that the H.E.S.S. light curve had only one significant flux point, representing the emission peak, and spanned 20 % of the orbit. It is necessary to resolve the H.E.S.S. light curve to isolate the emission peak. The physical implications of the orbital parameters are explored in van Soelen et al. (2018), wherein Inverse Compton Scattering, gamma-gamma absorption and Doppler boosting are modelled in an attempt to reproduce

the observed H.E.S.S. light curve.

The result shows that the addition of gamma-gamma absorption and Doppler boasting does shift the peak of the emission closer to the peak of the observed emission; nevertheless, more modelling is required.

The proposed research will resolve the light curve in the region with significant emission to tighten constraints on models since where the emission implies the physical processes at play.

1.3 Research Question

The initial study used 277 hours of data(Abdalla et al. 2018). Since then, the dataset has increased to 371.8 hours, and the system's orbital parameters have been determined; hence, the TeV light curve can now be resolved. Succinctly put, the question this research is answering is: *What orbital phase do we see the peak of the TeV emission?* The 20 % peak zone includes inferior conjunction (when the compact object passes in front of the star) which according to van Soelen et al. (2019), occurs at $\phi = 0.24$. This places inferior conjunction in the window of the H.E.S.S. phase bin where the emission peak is seen. However, since the phase bin spans $\phi = 0.2 - 0.4$, this extensive range leaves room for the possibility of the emission being before, at or after inferior conjunction.

It is essential to know where the peak of the TeV emission is because it is indicative of the physical processes involved, the extent to which they modulate the emission, whether we have the correct orbital solution and so on.

For instance, inverse Compton scattering is likely the dominant process for the GeV emission. The parameters that influence IC scattering predict the emission peak at superior conjunction (when the compact object passes behind the star), close to where we see the Fermi-LAT peak. This phase of the orbit is not where we see the peak of the H.E.S.S. light curve. So, what are the additional factors modulating the

TeV emission? This question brings us to the hypothesis of this work: **Gamma-gamma absorption modulates the inverse Compton TeV flux such that the peak of this emission occurs at inferior conjunction**[1]**.**

1.4 Research Aims and Objectives

The source of concern in this study is the binary LMC P3, an innately variable source. Hence, it is expected that the results will show some divergence from the previously published results. However, there may be variations, not necessarily physical, that could affect the results. To ensure that the results for LMC P3 are reliable, we will use N157B as a standard candle. N157B is a pulsar wind nebula (PWN) with a flux of about 2% of the flux of the Crab Nebula that is detected in yearly subsets of the LMC, which makes it an ideal object to use as a standard candle for the LMC (Komin et al. 2020).

Hence, one of the study's objectives will be to produce a spectrum compatible with the previously published H.E.S.S. spectra. We will also need to check that the flux from this source shows a constant flux to not lead to false conclusions of the variability of LMC P3.

1.4.1 Research Aim

To produce a spectral and temporal analysis of the gamma-ray binary LMC P3 with the updated H.E.S.S. dataset and orbital parameters.

1.4.2 Objectives

The objectives of the study are:

- to produce a spectrum for N157B compatible with the previously published spectrum.
- to check if the flux of N157B is constant

[1] This is also expected if the emission is of Inverse Compton Scattering origin but with a cone-like geometry of the system (similar to that proposed by Chernyakova et al. (2020), Fig.5.)

- to produce a spectrum for the complete orbit of LMC P3.
- to produce spectra for parts of the orbit which show significant emission.
- to produce flux measurements at different parts of the orbit resulting in a phase-folded light curve with 2 to 3 flux points.
- to compare the model for gamma-gamma absorption and inverse Compton scattering to the flux points.

1.5 Limitations

1.5.1 Sensitivity

The full orbit of LMC P3 has previously shown a flux of $(1.4 \pm 0.4) \times 10^{-13}\text{cm}^{-2}\text{s}^{-1}$ above 1 TeV (Abdalla et al. 2018). During the parts of the orbit where H.E.S.S. has seen no significant emission, the upper limits are set to $< 8.8 \times 10^{-14}\text{cm}^{-2}\text{s}^{-1}$ at the 95 % confidence level. These fluxes approach the H.E.S.S. sensitivity threshold (Holler et al. 2015a); thus, it is unlikely that this study will be able to probe the entirety of the light curve, even with the increased observation time.

1.5.2 Physical Modelling

There are many intricate models in the literature covering the array of physical processes that produce and modulate the observed gamma-ray flux, including, but not limited to, inverse Campton scattering, pion decay, electron-positron annihilation and cascades, gamma-gamma absorption, Bremsstrahlung and relativistic Doppler boosting, e.g. Dubus (2013). Due to time constraints and the scope of the study, only orbitally modulated Inverse Compton scattering will be tested, and gamma-gamma absorption will be discussed.

1.6 Outline

This chapter gives the reader a brief overview of what the study's aims are and what the significance and limitations of the study are. In Chapter 2, we will be

doing a literature survey to outline the current state of research and the theory of gamma-ray production. In chapter 3, we will cover the needed information about H.E.S.S., the Cherenkov detection technique, and the methodology employed in the data analysis. Then, chapter 4 will report the findings, which we discussed in chapter 5. Finally, chapter 6 will conclude and give recommendations for further study.

Chapter 2

Literature Review

This study aims to produce a VHE gamma-ray analysis of the gamma-ray binary LMC P3. In this chapter, we will look at the relevant theoretical and observational literature to understand the results obtained from the data analysis. This review will be geared towards understanding the VHE emission. However, aspects involving the multi-wavelength picture of gamma-ray binaries will be briefly explored. We will discuss the division in the literature regarding the scenarios for emission from binaries, how this affects the interpretation of the gamma-ray emission and what can be done to bring clarity to the situation.

2.1 Scenarios for Emission

Gamma-ray binaries consist of a massive star and a compact object. The compact object is either a black hole or a pulsar. But how does the interaction between these components produce gamma rays?
The two main scenarios for emission are that these systems are either powered by accretion or by the spin-down power of the pulsar (Dubus 2013). In the accretion scenario, the energy is supplied by releasing the gravitational potential energy of the infalling matter from the stellar companion to the compact object. In the pulsar wind scenario, the energy is supplied by the spin-down power of the pulsar.
The canonical explanation of gamma-radiation from binary systems is attributed to the microquasar scenario. Still, the investigation by Dubus (2006b) has shown that the pulsar wind scenario is plausible in systems now considered gamma-ray binaries. Both emission scenarios are shown in Figure 2.1.

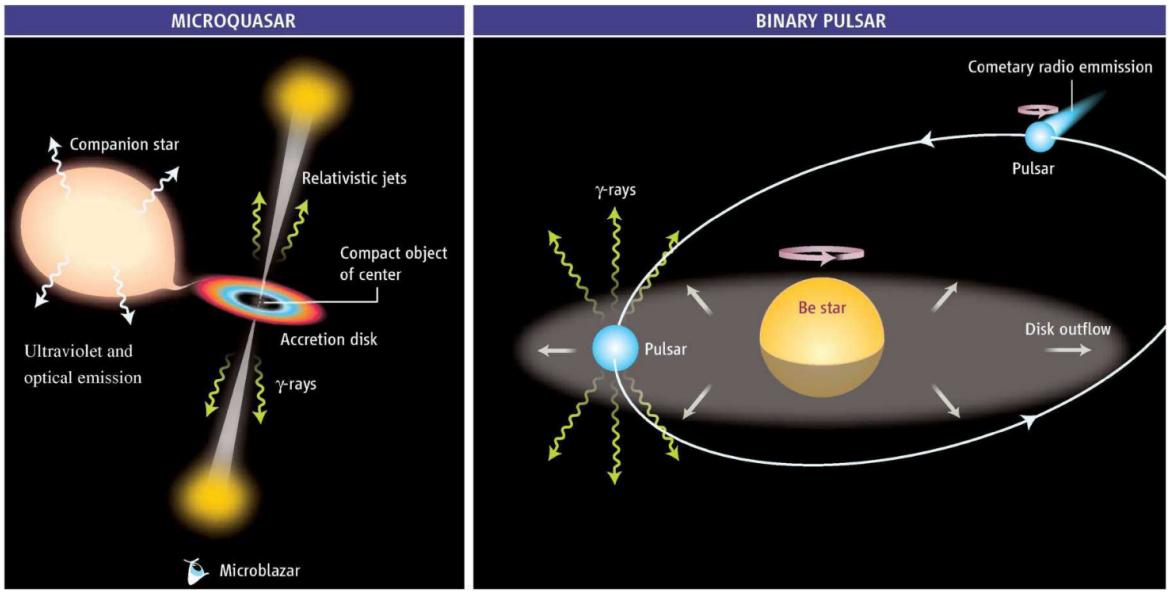


FIGURE 2.1: **Left:** The microquasar-jet model. Matter from the companion star is accreted onto the neutron star or black hole, producing relativistic jets which produce gamma rays. **Right:** The pulsar scenario where the wind from the pulsar interacts with the stellar environment from the companion to produce the gamma rays. **Source:** Mirabel (2007)

2.1.1 Microquasar Scenario

Active Galactic Nuclei (AGN) are known extragalactic sources of gamma-radiation from MeV to TeV energies. The emission is linked to relativistic jets powered by accretion onto the central supermassive black hole in the host galaxy (Dermer & Giebels 2016). Microquasars are galactic sources which operate on the same principle of jet power with the benefit of smaller temporal and spatial scales (Aharonian 2004). This interpretation has been historically used to explain emission in gamma-ray binaries (see, e.g. Khangulyan et al. (2007). The massive stellar companion donates mass to the compact object, forming an accretion disc and a relativistic jet believed to be the source of the gamma-ray emission (Aharonian 2004). This interaction is depicted in Figure 2.1.

2.1.2 Pulsar Wind Scenario

Neutron stars are born in supernova explosions of ordinary stars, which leave behind a dense remnant, mainly consisting of neutrons. Pulsars are rapidly rotating magnetised neutron stars(Aharonian 2004). Relativistic particles escape as pulsar wind beyond the pulsar's light cylinder ($R_L = cP/2\pi$). The light cylinder radius is the point at which the rotational velocity of the material tied to the magnetic field lines reaches the speed of light and decouples. In isolation, this wind collides with the interstellar medium (ISM), forming a pulsar wind nebula (PWN). In a binary system with a star, this wind collides with the stellar outflow forming a shock front. The shock front can accelerate relativistic electrons from the compact object's outflow to even higher energies. The relativistic electrons do Inverse Compton scattering off the stellar photon field, and this results in inverse Compton emission(Aharonian 2004). This interaction is summarised in Figure 2.1. This is the case in PSR B1259-63 (Dubus 2006b; Kirk et al. 2009).

2.2 The Compact Object

The questions related to the emission principle and the class differences between binaries can be answered by identifying the compact object. A minimum mass of $>3M_{\odot}$ would rule out a pulsar, in favour of a black hole, and detection of pulsations would confirm a pulsar. Direct detection of pulsations and firm mass measurements are elusive, so there is heavy reliance on indirect evidence of either scenario (Dubus 2013). Currently, the observational evidence, outlined in Section 2.2.1, favours the pulsar wind scenario.

2.2.1 Indirect Evidence for the Pulsar wind Scenario

A pulsar powers PSR B1259-63 and H.E.S.S. (Aharonian et al. 2005b) have detected luminous, orbital variable VHE emission. It has spectral and timing characteristics similar to other gamma-ray binary systems HESS J0632+057, LS I +61°303, 1FGL J1018.6–5856 and LS 5039, suggesting they could all be powered by the spin-down of a pulsar (Dubus 2013). Pulsars also have characteristically high gamma-ray luminosities, and gamma-ray binaries have steep VHE spectral indices($\Gamma_{VHE} \approx 2.7 - 2.4$), compatible with young pulsar wind nebulae (Dubus 2013). The spectral

similarity of PSR B1259-63 to that of LS 5039 and LS I+61°303 has been studied by Dubus (2006b) leading to the robust argument of uniting them and, by extension, gamma-ray binaries under the umbrella of being pulsar wind-driven systems. The study successfully reproduced the SED (spectral energy distribution) features of LS 5039 and LS I+61°303 in the pulsar wind framework.

The system LS 5039 is a system that is most similar to LMC P3, in that they both have relatively shorter periods (3.9 days for LS 5039 and 10.3 days for LMC P3). Both have their peak VHE emission near inferior conjunction, indicating similar physical scenarios (Aharonian et al. 2006b; Corbet et al. 2016; Abdalla et al. 2018). The caveat is that detectable emission has only been seen thus far in the phase bin corresponding with inferior conjunction for LMC P3, while LS 5039 shows detectable emission throughout its orbit. The resolved radio emission eludes to blazar-like jets from LS 5039 and LS I+61°303. A blazar is an AGN with its jet oriented close to the line of sight. However, pulsars and their interaction with the surrounding medium could also lead to large-scale emissions resembling a comet tail that can appear to be a jet (Dubus 2006b). LS I+61°303 and PSR B1259-63 have similar radio outbursts linked to their Be companions. In addition, all three have similar SEDs suggesting the same physics in these binary systems.

LS 5039 is thought of extensively in the literature to be a microquasar. Its high-energy emission is described and attributed to its nature as a microquasar (Paredes et al. 2000; Aharonian et al. 2006b, 2005b; Bosch-Ramon & Khangulyan 2009) to name a few.

Casares et al. (2005) not only suggesting that this system is accretion driven but also proposing that the system contains a black hole.

The model put forward by Albert et al. (2006) argue that a microquasar scenario over a previously suggested pulsar scenario is more favourable for the LS I +61 303 system since radio jets were detected; however, a few magnetar-like bursts have been detected (e.g. from *Swift* (Torres et al. 2011)). More recently, radio pulsations from LS I +61° 303 have been detected by Weng et al. (2022), making it the third gamma-ray binary with a confirmed pulsar as the compact object companion.

When it comes to the nature of the compact object, optical spectroscopy alone could not decide between a neutron star or a black hole companion for LS 5039.

Signs of accretion would confirm the blazar/microquasar scenario, but there are no conclusive signs. The systems have variability in X-ray and radio but not the robust

and fast variability expected in accreting HMXB, along with a lack of typical X-ray spectral cut-offs and atypical stable gamma-ray spectra. This evidence leads Dubus (2006b) to suggest that accretion does not occur in LS 5039 and LS I+61°303.
The characteristics of LS 5039 and LS I+61°303 indicate a young ms pulsar, and Dubus (2006b) shows that there is no present evidence against this. A young pulsar can push out material trying to accrete onto the pulsar. Radio pulsations are not possible due to the solid free-free absorption of the stellar winds, but the detection of X-ray/GeV pulsations is possible.

Using a pulsar wind model similar to PSR B1259-63, with different orbital parameters to match LS 5039 and LS I+61°303, Dubus (2006b) can sufficiently reproduce most of the properties in all three systems. The predicted spectral breaks match the observed SEDs of all three systems, and the small-scale radio emission are reasonably reproduced. The model does have the short-coming of not explaining the GeV emission of LS 5039 and LS I+61°303 and the radio outbursts in LS I+61°303 and PSR B1259-63, but overall, the model presents a unified, viable and supported framework to unite these systems under a common physical framework. This argument, in addition to the radio pulsations found in LS I+61°303 makes this framework even more viable.

2.2.2 Gamma-ray Binaries vs X-ray binaries

Gamma-ray binaries: A Proposed Definition

Dubus (2015) uses the term gamma-ray binaries to describe systems powered by pulsar rotation for reasons that will hopefully be made clear by the end of this chapter. The motivation for them to be treated as a separate class is motivated by the last two decades of gamma-ray observations (Dubus 2015). The consequence of gamma-ray binaries being a relatively new astrophysical class means the contours of the class are not fixed. Dubus (2015) points out that the term is sometimes used in literature to designate all binaries that have been detected in HE or VHE gamma-rays as a gamma-ray binary, which is too broad, sometimes it encompasses only high-mass gamma-ray binaries, which turns out to be too restrictive, and sometimes

adds microquasars in the definition, which mixes very different powering mechanisms and phenomenology. The proposed definition is systems with spectral energy distribution above 1 MeV(Dubus 2013) exhibit variable gamma-ray emission, sometimes modulated on the orbital period. This definition includes low-mass and high-mass binary systems. I will focus on high-mass systems for this study since LMC P3 falls under this category.

A list of systems that meet the criterion of high-mass gamma-ray binary according to the definition proposed (Dubus 2013), with the addition of LMC P3 is,

- PSR B1259–63, Oe star companion
- HESS J0632+057, Be star companion
- LS I +61$\circ$303, Be star companion
- 1FGL J1018.6–5856, O star companion
- LS 5039, O star companion
- PSR J2031+4127, Be star companion
- LMC P3, O star companion.

X-ray binaries

X-ray binaries comprise a neutron star or a black hole orbiting a stellar companion. This companion can have a range of masses, but for this discussion, I will be focusing on high-mass X-ray binaries (HMXB) wherein the stellar companion has a mass of $\geq 10\ M_{\odot}$. The x-ray emission has been attributed to hot accreting plasma, but the discovery of relativistic jets led to revisions on the basic concepts in X-ray binaries. It is established that jet power can be comparable or exceed the thermal luminosity (Aharonian 2004).

Commonalities in Accretion and Pulsar Wind Driven Systems

Both scenarios have the commonality that their non-thermal emission is linked to relativistically moving plasma coupled with compact objects - neutron stars and

black holes. The theory of relativistic collimated outflows is very complex and not yet adequately understood, dealing with magneto-hydrodynamics (MHD), electrodynamics, and strong shock waves with particle acceleration (Aharonian 2004).
There is believed to be an evolutionary link between high-mass X-ray binaries and Gamma-ray binaries: a young pulsar has strong enough wind to prevent accretion, and the pulsar spin-down power produces the observed high gamma-ray fluxes, and eventually, the rotation slows, and the pulsar wind pressure becomes insufficient to prevent accretion, so the system enters its high-mass X-ray binary phase (Dubus 2015).

Differences in Accretion and Pulsar Wind Driven Systems

A review by Dubus (2013) distinguishes accretion-powered HMXB and gamma-ray binaries summarised in Table 2.1. It should be noted that in the table, the specific definition of gamma-ray binary outlined above is used. It does not include all binary systems that emit gamma-rays such as SS 433, Cyg X-1, Cyg X-3.

TABLE 2.1: Assuming that gamma-ray binaries can be unified as all having a radio pulsar.

High-mass X-ray Binaries	**High-mass Gamma-ray Binaries**
Rarely have radio emission	Radio emission
Have curved X-ray spectra and X-ray pulsations	Hard X-ray spectra with no cutoff up to 100 keV (Dubus 2010)
Reach higher X-ray luminosities	Modest X-ray fluxes
Almost all have a neutron star, with a few having a black hole candidate	(assuming) Radio pulsar
Accretion-driven: plasma follows magnetic field lines to the poles resulting in x-ray pulses	No accretion: pulsar wind in these systems is too strong, forming a shock front
No coherent radio pulsations: Infalling material shorts the electric field	Non-thermal emission from high-energy particle acceleration at the shock, making them scaled-down pulsar wind nebulae

2.3 LMC P3: The Extra-galactic Gamma-ray Binary

2.3.1 The LMC Neighbourhood

The LMC is an irregular satellite galaxy of the Milky Way at a distance of 50 kpc (Pietrzyński et al. 2013).
There are currently four point-like VHE gamma-ray sources in the LMC, N 157B (a pulsar wind nebula), N 132D (a supernova remnant), 30 Dor C (a superbubble) and LMC P3(or CXOU J053600.0-673507; a gamma-ray binary) identified by H.E.S.S. (Komin et al. 2020). N 157B is the brightest source in the LMC with a flux of about 2% of the Crab Nebula and is detected in yearly subsets of the LMC and can be used as a standard candle (Abramowski et al. 2012; Collaboration 2015; Komin et al. 2020).

2.3.2 LMC P3 as an X-ray source

Bamba et al. (2006) did detailed X-ray observations of the supernova remnant DEM L241 with XMM-Newton, finding a point-like source with characteristics of a pulsar or a pulsar wind nebula (PWN). In an attempt to resolve the pulsar or PWN, Seward et al. (2012) found a high mass X-ray binary instead with Chandra in 2011 observations. The steep power-law spectrum of $\Gamma_X = 1.28 \pm 0.08$ lead them to believe the system was a high-mass binary system. The binary consists of an O-type star but no sign of a PWN. The hard power law spectrum suggests a pulsar as the compact object companion, but the observations did not show regular pulsations.

2.3.3 Gamma-ray detections from LMC P3

The first detection of gamma-ray emission from the system was established with Fermi-LAT Pass 7 reprocessed data(Ackermann et al. 2016), where a complete spatial and spectral model was developed using 73 months of data. This study labels the system as "P3", hence the name LMC P3. The system showed a very soft power-law spectrum, with index $\Gamma = 2.8 \pm 0.1$.

The system was then identified as a gamma-ray binary with a search for periodic emission using Fermi-LAT data, the first gamma-ray binary identified outside of

the Milky Way (Corbet et al. 2016). Its period was found to be 10.301 ± 0.002 days.

H.E.S.S. detected LMC P3 in TeV gamma-rays (Abdalla et al. 2018). It was found that the emission peak is in the phase bin 0.2 - 0.4. The 0 of the phase is defined at the Fermi-*LAT* maximum, set at MJD 57410.25 ± 0.34. The orbit modulates the VHE emission but is anti-phase with the HE (Fermi-*LAT*) emission. This is illustrated in Fig. 2.2. The VHE and HE lightcurves and their modelling can help to understand particle acceleration and gamma-ray production in the system.

2.3.4 Broadband emission

X-ray, radio and gamma-ray emission of LMC P3 is modulated by the orbital period of 10.3 days. These light-curves are shown in Fig. 2.3. The X-ray and radio emission is seen to be anti-phase with the HE gamma-ray emission. LMC P3 is more luminous in gamma rays than similar systems in the Milky Way. The radio emission is characteristic of gamma-ray binaries but uncommon for HMXB. The optical velocity measurements from Corbet et al. (2016) and van Soelen et al. (2019) suggest that a pulsar is preferred for the range of best-fit inclinations. A black hole is still possible for lower inclinations ($i \leq 15 \pm 2^{\circ}$) of the orbit.
Abdalla et al. (2018) detected VHE gamma-rays from LMC P3 and found a correlation between the X-ray and TeV light curves. There are discussions that in gamma-ray binary systems, correlations of X-ray and VHE emission are due to the energy of an electron population required to produce keV X-rays via synchrotron radiation being similar to the energy of an electron population required to produce VHE gamma rays via IC scattering (Zabalza de Torres 2011).

2.4 Relativistic Electrons' VHE Gamma-ray Production and Absorption

Inverse Compton scattering is especially effective in the VHE gamma-ray production regime as the Compton cooling time decreases linearly with energy (Aharonian 2004). IC scattering is the dominant VHE production in gamma-ray binaries (Khangulyan et al. 2014). Absorption via gamma-gamma pair production goes

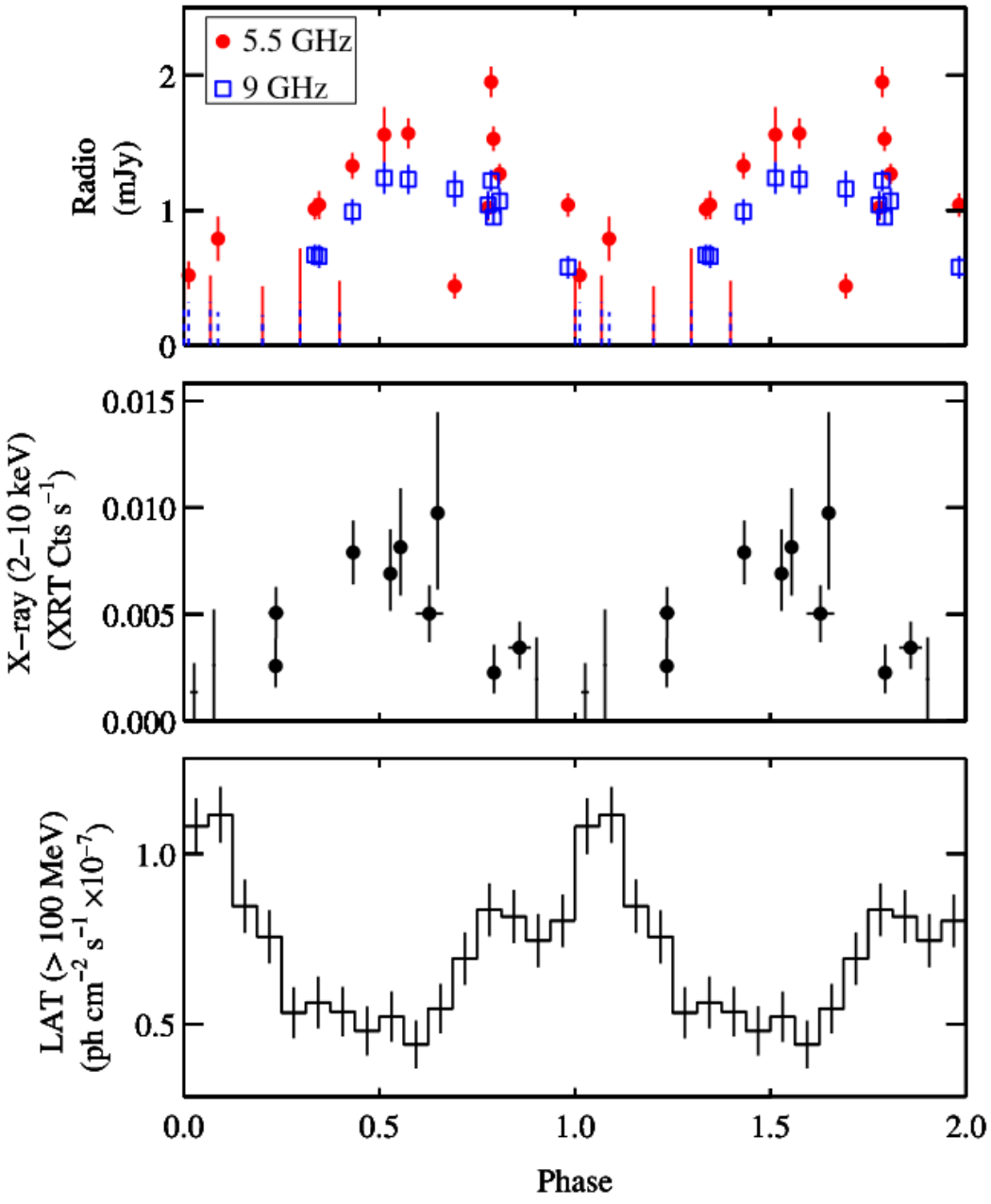


FIGURE 2.2: This plot shows the Radio (Top panel), X-ray (Middle panel) and HE gamma-ray light curves. Source: Corbet et al. (2016)

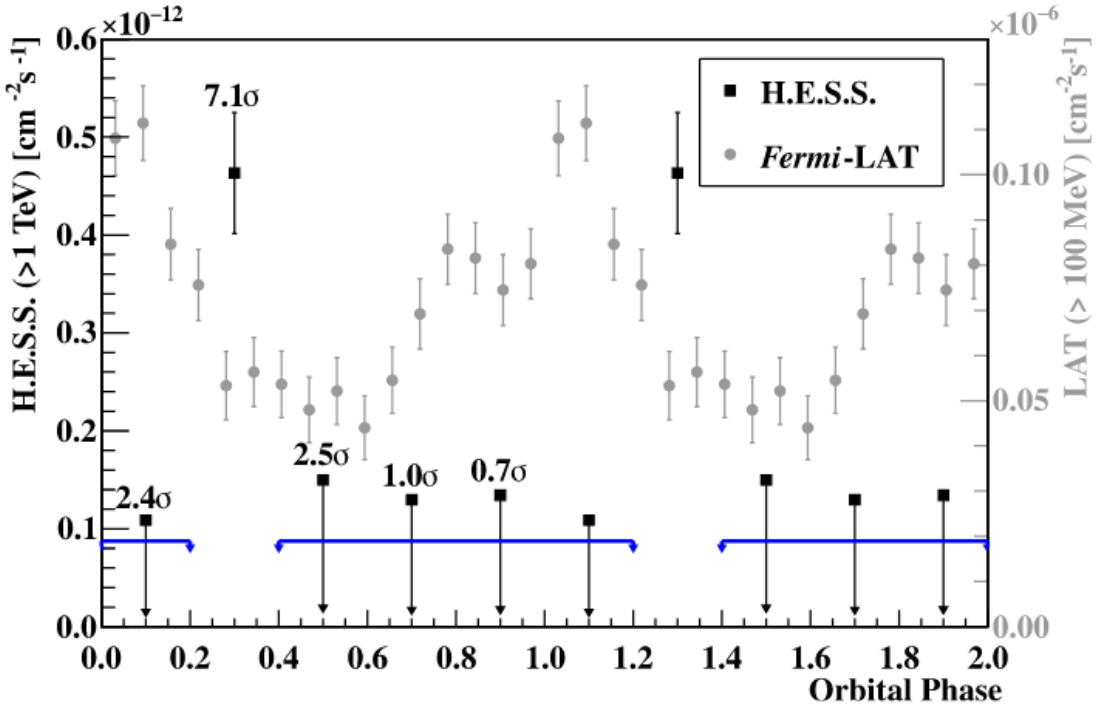


FIGURE 2.3: This plot shows the VHE phase folded light curve (black) imposed on the Fermi-*LAT* curve. Source: Abdalla et al. (2018)

hand in hand with IC scattering, as this process prevents the escape of energetic gamma rays in compact sources such as gamma-ray binaries (Aharonian 2004).

2.4.1 Inverse Compton Scattering

Compton scattering occurs when a photon interacts with a particle of matter, such as an electron, transferring some of its energy and momentum to the electron. Traditionally, the Compton effect occurs with the photon losing energy to the stationary electron (Longair 2010).

From the kinematics of an electron scattering with a photon at a scattering angle θ yields the Compton scattering formula (not derived here),

$$\epsilon_s = \frac{\epsilon}{1 + \frac{\epsilon}{m_e c^2}(1 - \cos\theta)}$$

where ϵ_s is the scattered photon energy and ϵ is the initial photon energy.

Inverse Compton scattering occurs when the electron has sufficient energy to transfer to the photon (Rybicki & Lightman 1991), resulting in up-scattered photons at the expense of the electron's kinetic energy (Longair 2010). In this case, transforming to the electron's rest frame allows the use of the Compton scattering formula. This boosts the photon's energy. For low-energy photons scattering off electrons at rest results in classical coherent Thomson scattering, where the photon's energy does not change after the interaction (Longair 2010). This relation is a good approximation as long as the photon's energy in the electron's rest frame is $\epsilon' \ll m_e c^2$ (Blumenthal & Gould 1970).

However, going from the lower energy electrons to ultra-relativistic electrons, quantum effects arise due to the exchange of energy and momentum between the photon and electron and as a result, the cross-section alters from the classical Thomson cross-section $\sigma_T = \frac{e^4}{6\pi\epsilon_0^2 m_e^2 c^4}$ to the Klein-Nishina cross-section,

$$\sigma_{KN} = \pi r_e^2 \frac{1}{x}\left\{\left[1 - \frac{2(x+1)}{x^2}\right] + \frac{1}{2} + \frac{4}{x} - \frac{1}{2(2x+1)^2}\right\}$$

where $x = \frac{\epsilon}{m_e c^2}$ and $r_e = \frac{e^2}{4\pi\epsilon_0 m_e c^2}$ (Rybicki & Lightman 1991; Longair 2010). In the limit $x \gg 1$, $\sigma_{KN} = \pi r_e^2 \frac{1}{x}\left(\ln 2x + \frac{1}{2}\right)$ Hence, with ultrarelativistic electrons, the cross-section decreases.

The Klein-Nishina regime is where we see the production of TeV photons, this is the energy range pertaining to this study. This relationship is illustrated in Fig. 2.4. The change in gradient in the produced photon energy illustrates the shift from the Thomson to the Klein-Nishina regime. This shift is explained by the fact that as the electron gets more relativistic, it loses a larger portion of its energy to a photon in individual scatters, resulting in the energy of the scattered photon depending less on its initial energy and more on the energy of the electron (Blumenthal & Gould 1970).

The UV photon energy used in the production of Fig. 2.4 is ≈ 6 eV and to produce a TeV photon, an electron of at least $\gamma \approx 10^5$ is required (Paredes & Bordas 2019). Considering a head-on collision, the relationship between the photon's energy in the electron's rest frame and the observer frame is, $\epsilon' = (1+\beta)\gamma\epsilon$ and using $\beta \approx 1$ gives $\epsilon' = 2\gamma\epsilon$ (Bradt 2008), so using the values from Paredes & Bordas (2019), $\epsilon' \approx 12 \times 10^5$ eV $= 1.2$ MeV which is comparable to $m_e c^2 = 0.511$ MeV so this occurs in the Klein-Nishina regime.

In addition to energetic effects, IC scattering also depends on the incident angle of the electron on the photon. For a scattering angle of $\theta = 180^\circ$ (back-scatter) the maximum energy is transferred and it decreases as $\theta \to 0^\circ$. In gamma-ray binaries, the angle of the electrons from the pulsar and the photon field changes as the pulsar orbits the star, adding additional modulating effects.

The spectrum of the Inverse Compton scattered photons are of immediate interest as this is what is observed. However, many literary sources focus on the Thomson limit, e.g. Longair (2010); Rybicki & Lightman (1991); Bradt (2008). Blumenthal & Gould (1970) attempt to produce a generic form of the inverse Compton spectrum for an isotropic seed photon field and a power law electron distribution. However, the expression can only be evaluated in the Thomson and extreme Klein-Nishina limits.

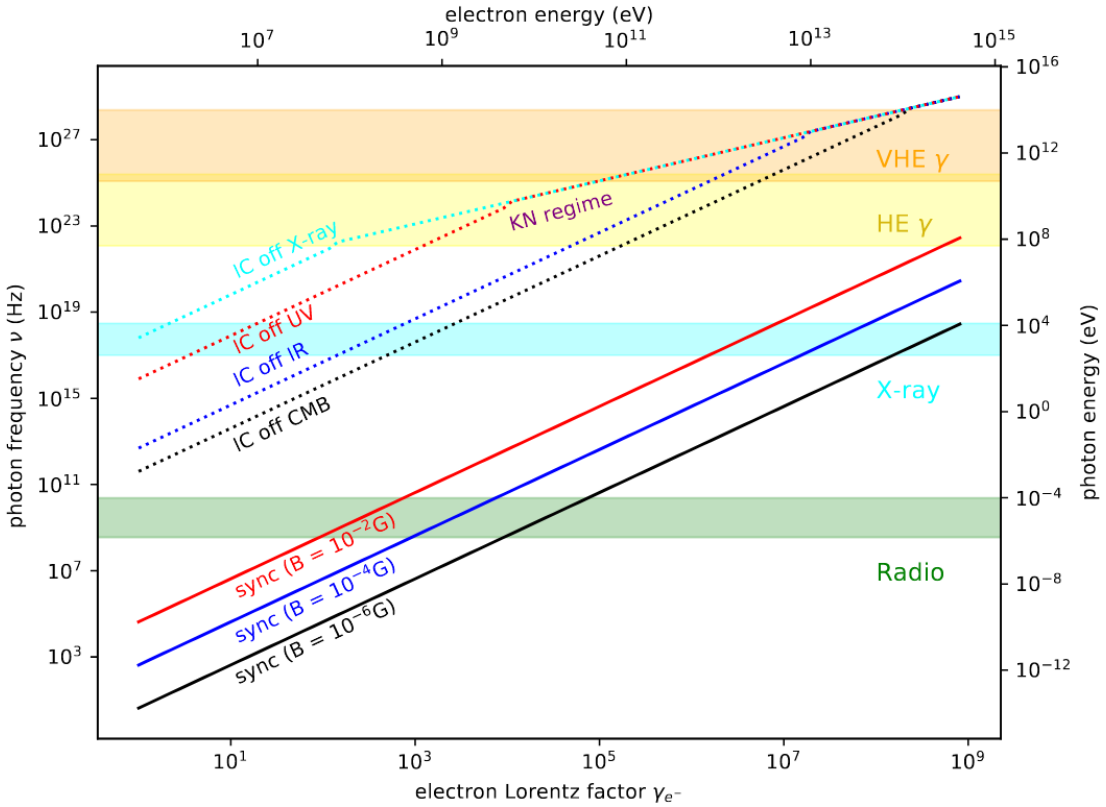


FIGURE 2.4: This plot shows the photon energy produced in the non-thermal processes (Synchrotron radiation and Inverse Compton radiation) for different seed photon energies and electron energies (or Lorentz factors). To produce TeV gamma-rays, an electron energy of at least $\approx 10^{11}$ eV is required for an X-ray seed photon. It can also be seen from the figure that in the Klein-Nishina regime, The energy of the IC photon depends less on the seed photon and more on the electron's initial energy. Source: Paredes & Bordas (2019)

A power-law distribution of electrons is produced in the most relevant acceleration processes in astrophysics (Aharonian & Atoyan 1981). For a power law distribution of electrons $\frac{dN_e}{d\epsilon_e} \propto \epsilon_e^{-\Gamma}$, the Klein-Nishina photon distribution has the behaviour $\frac{dN}{dE_\gamma} \propto \epsilon_\gamma^{-(\Gamma+1)}(\ln 4\omega_0\epsilon_\gamma + const.)$, where ω_0 is the energy of the seed photon (Aharonian 2004; Blumenthal & Gould 1970; Aharonian & Atoyan 1981). IN the KN regime the photons' spectrum slope differes from the slope of electrons by ≈ 1.
Aharonian & Atoyan (1981) has analytical approximations for gamma-ray spectra used in the software package *naima*(Zabalza 2015), which has been used in this study.
The energy loss rate of relativistic electrons in a monoenergetic photon field given by Aharonian & Atoyan (1981) is,

$$\frac{d\epsilon_e}{dt} = \frac{3\sigma_T c n_{ph}}{4\omega_0 b}\left[\left(6+\frac{b}{2}+\frac{6}{b}\right)\ln(1+b) - \ln^2(1+b) - 2\mathrm{Li}\left(\frac{1}{1+b}\right) - \frac{(11/12)b^3+8b^2+13b+6}{(1+b)^2}\right]$$

where $b = 4\omega_0\epsilon_e$ and $\mathrm{Li}(x) = \int_x^1 (1-y)^{-1}\ln(y)dy$. In the Thomson limit, this reduces to

$$\frac{d\epsilon_e}{dt} = \frac{4}{3}\sigma_T c\omega_o n_{ph}\epsilon_e^2$$

In the Klein-Nishina limit, this reduces to

$$\frac{d\epsilon_e}{dt} = \frac{3}{8}\frac{\sigma_T c n_{ph}}{\omega_0}(lnb - 11/6)$$

In the Thomson limit, this results in a steep electron spectrum, while in the Klein-Nishina regime, the electron spectrum is hard and almost energy independent(Aharonian 2004).

2.4.2 Photon-photon Pair Production/Gamma-gamma Absorption

Photon-photon (or gamma-gamma) pair production occurs when two photons interact and produce an electron and positron pair (Aharonian 2004). This process has a strict kinetic threshold of,

$$\epsilon_\gamma\epsilon(1-\cos\theta) \geq 2m_e^2c^4$$

where ϵ_γ and ϵ is the energy of two photons colliding at an angle θ in the lab frame. Considering a gamma-ray of energy $_\gamma = 511$ GeV, a stellar photon of $\epsilon \approx 1$ eV can pair produce with this gamma-ray, making gamma-gamma absorption a relevant process in modulating TeV gamma-rays. In the relativistic regime, photon-photon absorption behaves similarly to IC scattering (Aharonian 2004). This makes gamma-gamma absorption an important emission modulator in gamma-ray binaries and other compact sources.

In the case of gamma-ray binaries, it is required to express the kinetic threshold in general 3D vector form,

$$\epsilon_\gamma \epsilon (1 - \mathbf{e}_\gamma \mathbf{e}_\epsilon) \geq 2 m_e^2 c^4$$

where $\mathbf{e}_\gamma$ and $\mathbf{e}$ are directions of the two photons (Dubus 2006a). The interaction cross-section $\sigma_{\gamma\gamma}$ depends only on $s = \frac{\epsilon_\gamma \epsilon}{2 m_e^2 c^4}(1 - \mathbf{e}_\gamma \mathbf{e}_\epsilon)$ (Gould & Schréder 1967). So, the threshold for interaction is $s > 1$.
Gamma-gamma absorption is characterised by the opacity $\tau_{\gamma\gamma}$, and in gamma-ray binaries like LMC P3, the dominant radiative output is the massive star companion, which is assumed to have a blackbody radiation density with a temperature T_* and radius R_* given by

$$n_\epsilon = \frac{2\epsilon^2}{h^3 c^3} \frac{1}{\exp(\epsilon / k T_*) - 1} \text{ ph cm}^{-3} \text{ erg}^{-1} \text{ sr}^{-1} \tag{2.1}$$

For the point source approximation $R_* << d$ from Dubus (2006a) gives the differential opacity

$$d\tau_{\gamma\gamma} = \pi \left(\frac{R_*}{d} \right)^2 \sigma_{\gamma\gamma} n_\epsilon (1 + \cos\psi) dl d\epsilon$$

where ψ is the angle the gamma-ray makes with the negative z-axis, dl is a differential line segment.

Gamma-gamma absorption provides a novel way of seeing if VHE gamma-ray production occurs on small scales, i.e. the scales of the star and compact object separation or on larger scales, further away from the star and compact object. The dense photon field near the stellar companion acts as target photons that seed absorption.

The predictions made taking this into account can be used to distinguish between variability in gamma-ray production by IC scattering and gamma-ray absorption as it gets modulated along the orbit (Dubus 2006a). The predictable, repeatable modulation due to the orbital period of binary systems and the compact object probing different parts of the radiation field as it moves through its elliptical orbit allows this to be a reliable experiment to test theories of particle acceleration in the most extreme conditions.

Chapter 3

Research Methodology

3.1 Ground-based Gamma-ray Detection

This section will focus specifically on the ground-based gamma-ray detection technique, which is the method used by H.E.S.S. to detect VHE gamma rays.

3.1.1 Electromagnetic Air Shower

Pair Production and Bremsstrahlung

The pair production of a single gamma ray above the energy threshold of >1.02 MeV occurs when it interacts with the electric field of a nucleus, shown in Fig. 3.1. It is the predominant interaction of gamma rays greater than 10 MeV, making the atmosphere opaque in gamma rays (Weekes 2003). However, there is a gamma-ray window from about 100 GeV, which uses this interaction to detect gamma rays (and cosmic rays) with ground-based instruments. This lower limit is set by the sensitivity of the current generation of Imaging Atmospheric Cherenkov Telescopes (IACTs).
A primary gamma ray enters the atmosphere and pair produces to form an electron-positron pair, which then undergoes Bremmstrahulung. Bremsstrahlung occurs when an incident charged particle (in this case an electron or positron) is decelerated in the electric field of a nucleus and emits a photon proportionate to the energy loss(Weekes 2003). This interaction is depicted in Figure 3.2.

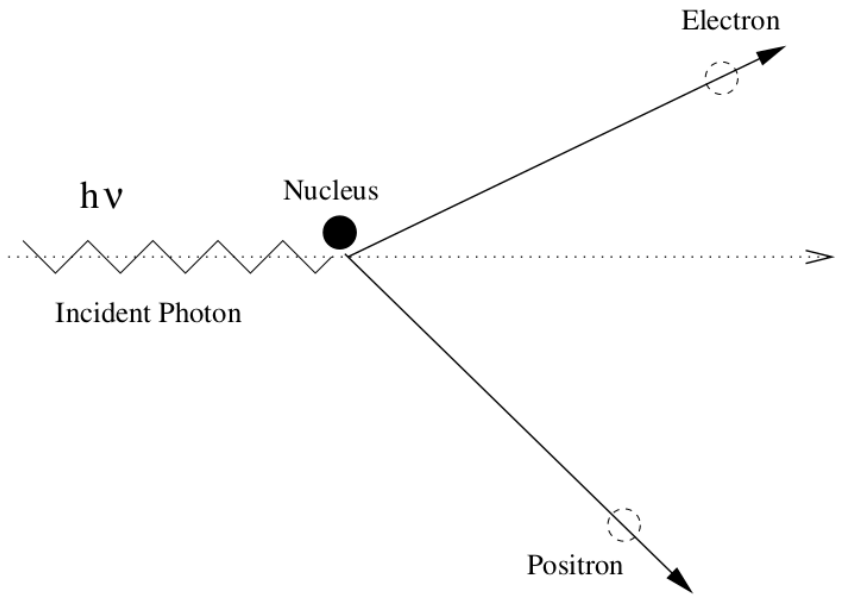


FIGURE 3.1: This plot shows the incident gamma ray interacting with a target atmospheric nucleus to annihilate and form an electron-positron pair. Source: Weekes (2003)

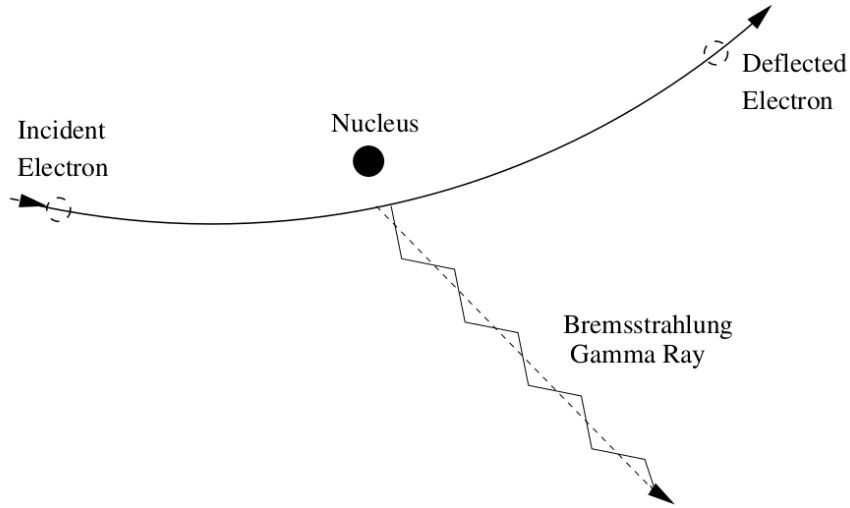


FIGURE 3.2: This plot shows the deflection of an electron interacting with a target atmospheric nucleus to produce a photon. Source: Weekes (2003)

This pair production process and Bremsstrahlung of the secondary electrons, positrons and gamma rays repeats down through the atmosphere, producing an *electromagnetic air shower.* The cascade stops when ionization and radiation energy losses are equal marking the *shower maximum* (Weekes 2003).

Hadronic Air Showers

Charged cosmic rays (mostly protons) interact with the atmosphere and create a similar particle cascade to gamma rays and form the background (this background may be more numerous than the expected gamma ray flux by a thousand times) in the Cherenkov detection technique (Weekes 2003). A proton emits its secondary particles at wider angles than gamma rays, so the particle cascade is wider (Weekes 2003) which is one way to differentiate the Cherenkov light pulses. The air showers are shown in Fig. 3.3.

3.1.2 Cherenkov Radiation

The majority of particles produced in the air shower are absorbed by the atmosphere and do not reach the ground. Cherenkov radiation occurs when a particle exceeds the speed of light in the medium it is travelling through. The threshold velocity for emission v/c > 1/n where v is the velocity of the particle, c the speed of light in the medium, and n, is the refractive index(Weekes 2003). In a time T, the relativistic particle travels a distance βcT and the photon emitted travels cT/n so the opening angle is defined as $\cos\theta = \frac{c/n}{\beta c}$ and for $\beta \to 1$,

$$\cos\theta = \frac{1}{n}$$

the reflective index in air is $n = 1.0003$, so the opening angle is ≈ 1.4 °. This is shown in Figure 3.4.

3.1.3 The H.E.S.S. Experiment

The High Energy Stereoscopic array (H.E.S.S.) is 1800 m above sea level, (23 °16′ 18″ South, 16 °30′ 00″ East) in the Khomas Highlands, Namibia (Aharonian et al. 2006a). The array of four initial telescopes (100 m^2 mirror area) are placed in a

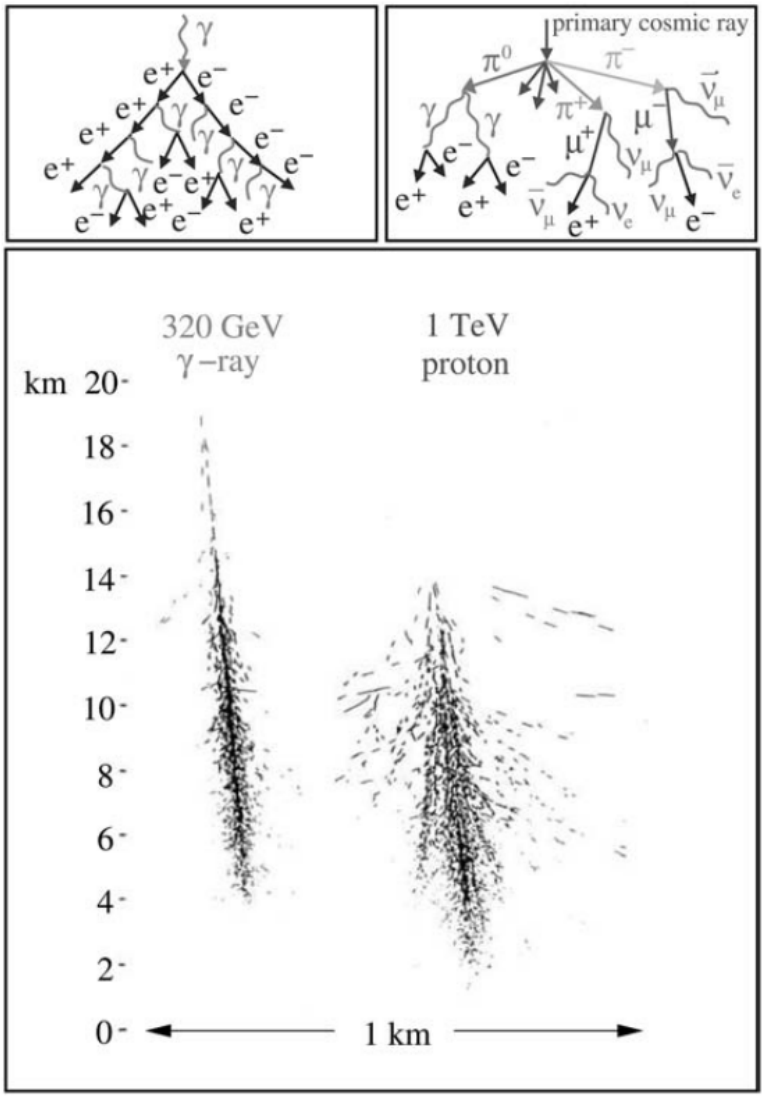


FIGURE 3.3: Top panels: Schematic development of a gamma-ray shower (left) and a proton shower(right). Main panel: Monte Carlo simulations of gamma-ray and cosmic proton showers. The tracks of some of the particles that emit Cherenkov light are shown. Source: Weekes (2003)

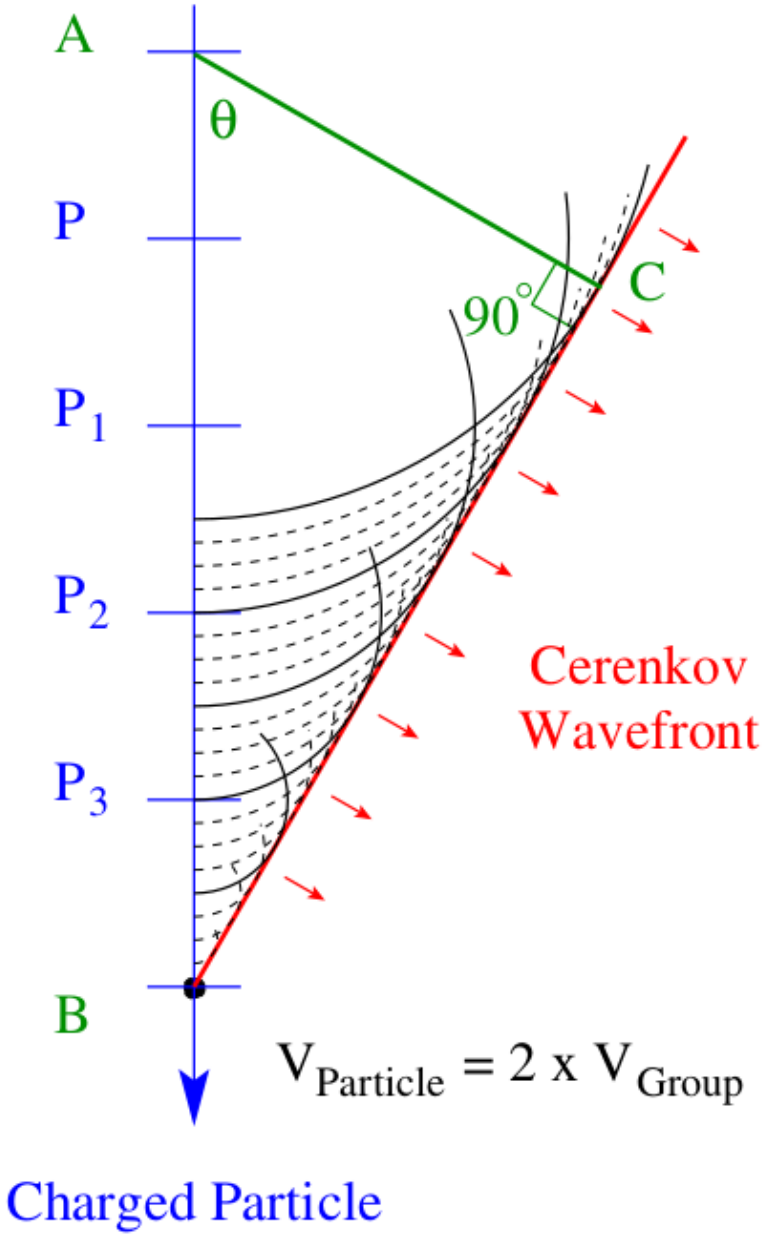


FIGURE 3.4: Cherenkov Radiation opening angle. Source: Weekes (2003)

square formation, side length 120 m, for an energy threshold > 100 GeV, and an additional 600 m^2 mirror area telescope in the middle, lowering the threshold to several tens of GeV (Holler et al. 2015b). These telescopes detect optical Cherenkov light.
The array of dished mirrors reflects Cherenkov light into cameras.

The detectors

The original four telescopes are named Cherenkov Telescopes 1 to 4 (CT1-4); the fifth telescope, added in 2012, is named CT5.
The Cherenkov telescopes consist of steel frames, and a mount that tracks a source across the sky, a dish consisting of 60 cm circular mirrors arranged in a hexagonal pattern that directs the Cherenkov flashes into the camera (Aharonian et al. 2006a).

The cameras consist of Photo-Multiplier tubes, which detect the photons and are directed to analogue memory (Naurois 2012). Then, the events are built and go through extensive calibration through the Data Acquisition (DAQ) pipeline, outlined in (Naurois 2012).

Gamma-ray Selection

In the Cherenkov technique, the majority of events that trigger the telescopes are cosmic ray triggers. It is critical to separate the cosmic ray triggers from the gamma-ray events, and additional methods must be employed to account for the reduction of the hadronic background during analysis.
The events undergo gamma-hadron separation and energy estimation by a software called "*Model Analysis*" outlined in De Naurois & Rolland (2009). In Model analysis, the real camera images are fit with simulated images, and events are selected based on the goodness of fit. The shower images are reconstructed for a single camera, then stereoscopically for multiple cameras to find the direction of the original gamma ray(Naurois 2012).

3.2 Data

Here, we describe the source of the data, which is the H.E.S.S. experiment, explain the observations used, and the pre-processing steps taken.

3.2.1 Observations of the Large Magellanic Cloud

This analysis forms part of an ongoing survey of the LMC by the H.E.S.S. Collaboration Legacy program. The dataset used consists of 1344 observation runs of the LMC from 2004 to 2022.

Pre-processing/Treatment of data

The datasets used in this analysis were converted to FITS files (Wells & Greisen 1979) and consist of γ-like events (events which are most likely gamma-rays, the majority of hadron-like events have been mainly filtered out). The FITS format is an n-dimensional data array format with an unlimited number of parameters used to describe and document the arrays developed in 1979(Greisen et al. 1980).
The files were created through the Paris Analysis (PA) pipeline using the propriety H.E.S.S. software.
The events were filtered by quality selection cuts. Depending on the analysis one wants, there are several ways the data selection can be done. For *H.E.S.S. I Stereo* modes, the events are reconstructed stereoscopically using only events seen by two or more CT1-4 cameras. *H.E.S.S. II Stereo* consists of events seen by a combination of CT5 and CT1-4 cameras[1]. The event-selection cuts, which reject the background events, are also specified. There is the *Standard* event selection cuts, *Faint* event selection cuts which are optimised for faint gamma-ray sources, *Loose* event selection cuts lessen the constraint on hadronic background separation, and *Very Loose* eases the constraints even more so. This is summarised in Table 3.1.
The reconstructed events are stored with instrument response functions (IRFs) produced from Monte-Carlo simulations. Events consist of the estimated position, energy and arrival time. IRFs consist of the effective area of the instrument, which is a function of true energy and offset angle from the field of view centre (response is

[1]Other modes can be used for instance *H.E.S.S. II Mono* (that only includes events seen by CT5) and *H.E.S.S. II Combined* (including *Mono* events and *Stereo* events but neither are used for this study.)

TABLE 3.1: H.E.S.S. analysis configuration modes.

Configurations	**Description**
H.E.S.S. I Stereo Faint	Stereoscopic events from CT1-4. Optimised for faint sources.
H.E.S.S. I Stereo Standard	Stereoscopic events from CT1-4. Standard cuts applied.
H.E.S.S. II Stereo Standard	Stereoscopic events from CT1-5. Standard cuts applied.
H.E.S.S. I Stereo Loose	Stereoscopic events from CT1-4. Less background separation.
H.E.S.S. I Stereo Very Loose	Stereoscopic events from CT1-4. Less background separation.

weaker the larger the offset), energy dispersion, which corrects for the uncertainty in the reconstructed energy of the incident gamma-ray. These are dependent on the radial offset from the field of view centre, the energy of the gamma-ray, the zenith angle (and atmospheric conditions) and the camera and mirror efficiency. The energy dispersion relates the true energy of the gamma ray to the reconstructed energy.

3.3 Methods

3.3.1 Software Packages

The analysis is done in Gammapy version 0.20.1.
Gammapy (Deil et al. 2017) is an open-source gamma-ray astronomy Python package developed for use with existing gamma-ray telescopes and the Cherenkov Telescope Array (CTA), which is currently under construction for next-generation Imaging Atmospheric Cherenkov Telescopes IACTs. Gammapy is used for high-level analysis of reconstructed gamma-like events stored in FITS files and is built upon rigorously tested, commonly used python astronomy packages Numpy, Scipy and Astropy. It also makes use of the naima package (Zabalza 2015). Gammapy can create images, spectra and light curves and determine the position and morphology (for extended sources). Gammapy can also estimate background information for a source using the ring and reflected background method (Berge et al. 2007).

3.3.2 LMC Objects

The sources in the LMC are defined using fixed positions, defined in Table 3.2.

TABLE 3.2: Fixed position of point-like sources in the LMC in Galactic coordinates. The positions of these sources were used to define exclusion regions for background estimation.

Source	**Coordinates**
LMC P3	277.72421°, -32.08862°
N157B	279.55872°, -31.74586°
N132D	280.31°, -32.78°
DorC	279.6240°, -31.9118°
SN1987A	279.703427°, -31.937066°
Potential Emission	279.5458541°, -33.34244222°

N 157B Spectrum

N157B is the brightest source in the LMC; hence it is used as a standard candle to check the consistency of the analysis. To do so, the spectrum produced should be consistent with the published spectrum,

$$\frac{dN}{dE} = \Phi_0 \left(\frac{E}{1.5\text{TeV}} \right)^{-\alpha - \beta \times \ln\left(\frac{E}{1.5\text{TeV}}\right)}$$

with $\Phi_0 = (3.6 \pm 0.1) \times 10^{-9} \text{m}^{-2}\text{s}^{-1}\text{TeV}^{-1}$, $\alpha = (2.23 \pm 0.08)$ and $\beta = (0.32 \pm 0.07)$ (Komin et al. 2020). The gamma-ray luminosity in the 1-10 TeV range for a distance of 50 kpcs is $(6.5 \pm 0.3) \times 10^{35}$ erg/s.

LMC P3 Spectrum

The published best-fit parameters of LMC P3 is shown in Table 3.3. It is taken from Komin et al. (2017), and the result was not expected to match the published spectrum since the orbit is sampled differently in the updated dataset, hence the need to use the spectrum of N157B as a standard candle. The orbital phase 0 for LMC P3 is set to the Fermi-LAT maximum at MJD 57410.25 (Corbet et al. 2016).

LMC P3 Orbital Parameters

The orbital period found for LMC P3 from van Soelen et al. (2019) is 10.314 ± 0.044 d, consistent with Corbet et al. (2016)'s 10.301 ± 0.002 d. van Soelen et al. (2019)

TABLE 3.3: Statistical results and spectral parameters for different orbital phase bins of H.E.S.S. J0536-675. The on-peak region covers orbital phases from 0.2 to 0.4, and the off-peak region the orbital phases from 0.4 to 0.2. Orbital phase 0 is defined at the maximum Fermi-LAT emission at MJD 57410.25. Source: Abdalla et al. (2018)

Orbital phase bin	$\Phi_{\mathbf{1TeV}}$ $[10^{-13}\mathrm{cm}^{-2}\mathrm{s}^{-1}\mathrm{TeV}^{-1}]$	Γ	$\mathbf{F}\ (>1\mathbf{TeV})$ $[10^{-13}\mathrm{cm}^{-2}\mathrm{s}^{-1}]$	$\mathbf{L}(1-10\mathbf{TeV,\ 50\ kpc})$ $[10^{35}\mathrm{erg\ s}^{-1}]$
Full orbit	2.0 ± 0.4	2.5 ± 0.2	1.4 ± 0.4	1.4 ± 0.2
On peak (0.2-0.4)	5 ± 1	2.1 ± 0.2	5 ± 2	5 ± 1
Off peak (0.4-0.2)	-	2.4(fixed)	<1.2(95% CL)	<1.2(95% CL)

adopts a value of 10.301 d to determine the other parameters. This was also the period adopted in this study. The orientation for the binary orbit shown in Fig. 3.5 was determined with an assumed optical star of mass $M_* = 33.5M_\odot$ and radius $R_* = 14.5R_\odot$ and a compact object mass $M_{co} = 1.4M_\odot$. Phase $\phi = 0$ following Corbet et al. (2016) is given to be at MJD = 57410.25, placing superior conjunction (when the star is in front of the compact object) at $\phi_{sup} = 0.98$ and inferior conjunction (when the compact object is in front of the star) at $\phi_{inf} = 0.24$ and periastron (when the compact object is closest to the star) $\phi_{per} = 0.13$.

The time of periastron in HJD is measured at 2457412.13 ± 0.29. The velocity semi-amplitude used is $k = (10.69 \pm 1.23)$km/s and the longitude of periastron $\omega = (11.3 \pm 12.0)$ deg. The eccentricity is set to 0.40 ± 0.07. The range of possible inclinations are given in van Soelen et al. (2019), but this study fixes the inclination at 90°.

3.3.3 Run Selection

The source position is set to N157B for the consistency check or LMC P3 in the primary analysis notebook. The analysis configuration is set to H.E.S.S. I Stereo Faint; H.E.S.S. I Stereo means only stereoscopic data from CT1-4 is used. CT5 is elected to be ignored to improve the agreement between this result and previously published values(Komin et al. 2020), as the data will be homogeneous. The Faint configuration is optimised for faint sources like LMC P3.

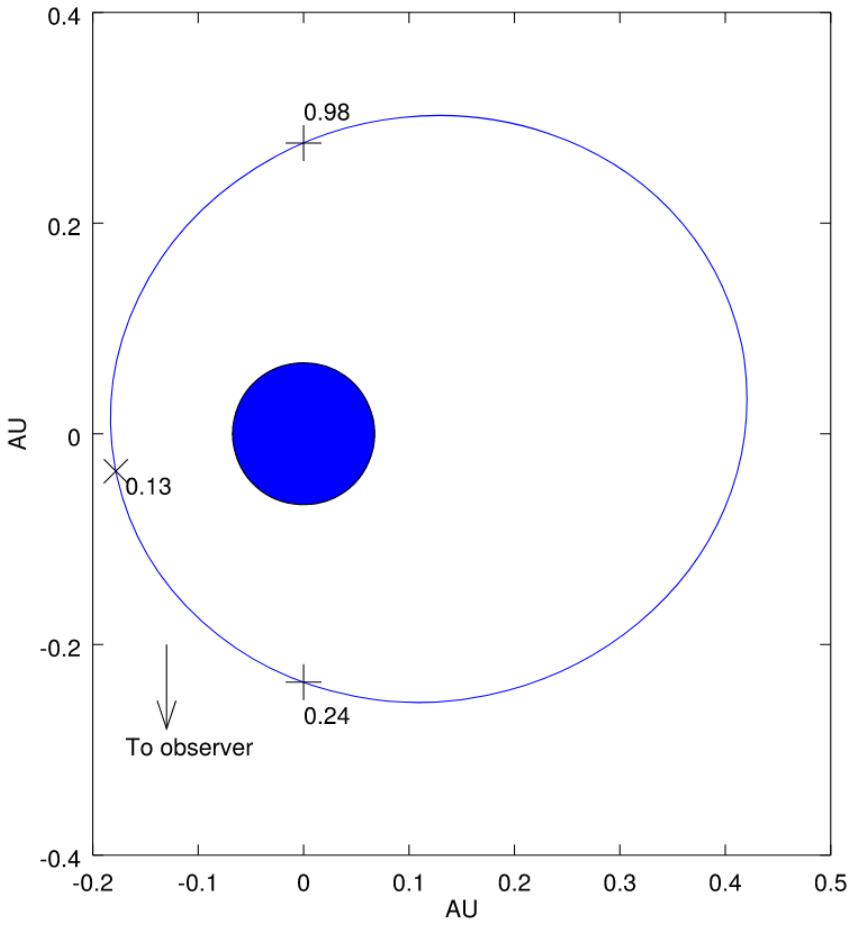


FIGURE 3.5: The binary orientation of LMC P3 showing the star (blue circle), positions of inferior and superior conjunction marked with a + and periastron $\times$. Source: van Soelen et al. (2019)

The cone search parameters are set to the direction of the source and a radius of 2.5°.
The LMC datastore is then filtered by the Gammapy analysis object for the observations that meet the cone search criteria. For N 157B, this results in 1281 runs and for LMC P3 this results in 1344 runs.

3.4 Analysis: Spectrum

3.4.1 Data reduction

The source is defined as a circular region with a radius of 0.1°around the source position (277.72421°, -32.08862°) for LMC P3 and (279.55872°, -31.74586°) for N 157B, as shown in Table 3.2. Next, the energy axis is specified from 0.1 to 40 TeV with ten energy bins, and the true energy axis is determined from 0.05 to 100 TeV with 20 bins. Next, the background is estimated using the reflected regions background method (Berge et al. 2007). Next, a safe mask is applied using a maximum effective area set to 10 % and a maximum offset angle of 2°. The dataset for each run was then stacked into a single stacked dataset, selecting for counts, exposure and energy dispersion (the IRFs). Finally, the source's cumulative signal and background were compiled into a table. The cumulative excess and the cumulative significance for the full orbit of LMC P3 plotted over the livetime are shown in Figures 3.6 and 3.7. For a non-variable source, with observations taken under similar conditions, the excess should have a linear relationship with livetime, and the significance (square root of the test statistic) should have the same evolution as a square-root function with respect to livetime. The reason these behaviours are not seen in Fig. 3.6 and 3.7 is twofold: the source is highly variable, so we expect to see a variation in source counts regardless of livetime, and (2) since this dataset contains the all the runs taken of the LMC in different observation positions, there are varying camera offsets meaning that a run that has LMC P3 close to the camera centre, would record more counts than a run where LMC P3 is further from the camera centre.

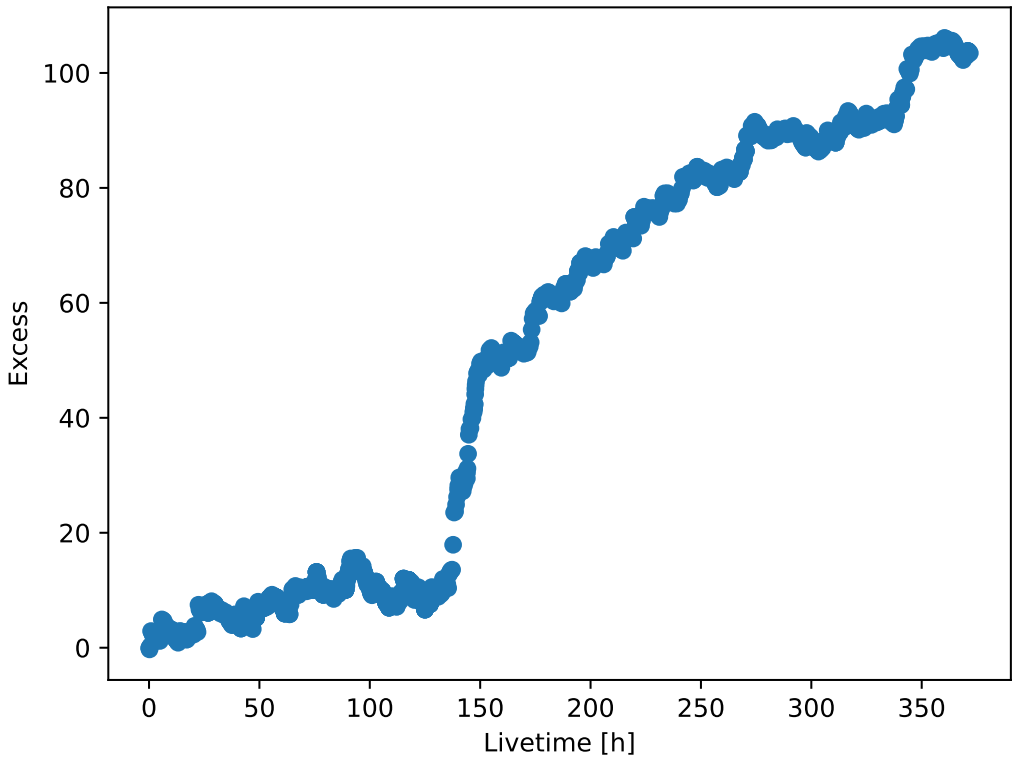


FIGURE 3.6: Plot of the cumulative excess of the full dataset of LMC P3 plotted over the livetime.

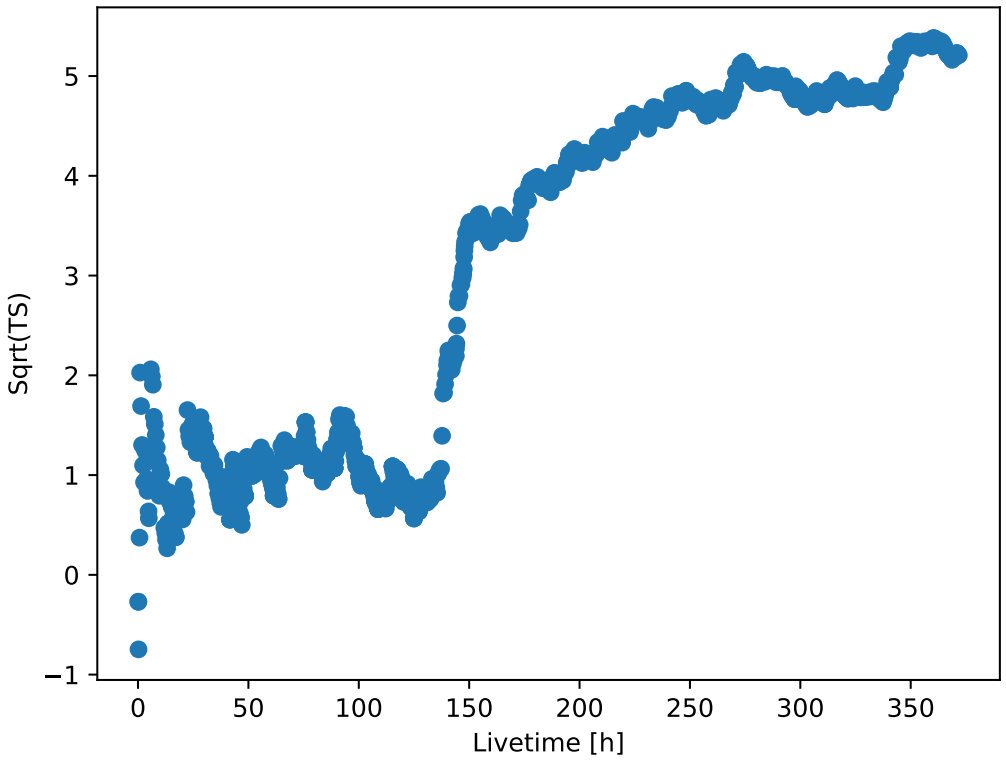


FIGURE 3.7: Plot of the cumulative significance of the full dataset of LMC P3 plotted over the livetime.

3.4.2 Spectral Fitting and Flux Estimation

The stacked dataset was then fit to a power law spectrum outlined above and a point source assumption. The spectrum was set to the stacked dataset and passed to the Fit object. The fit is done by folding the model prediction with the IRFs obtaining a model for the counts. The best-fit parameters are obtained by performing a maximum likelihood fit. After fitting the model, the excess counts were plotted against the model's predicted counts.
The fit and published spectrum were then plotted to compare the result to the established spectrum.
The flux points are estimated using the flux point estimator, across the energy range of the full dataset (0.6 - 40 TeV). These flux points are used to produce a plot of the spectrum. The flux was also estimated for a single bin between the energies 1 - 10 TeV.

3.5 Analysis: Sky Maps

The background estimation was done using the *ring background method*(Berge et al. 2007). The significance peak estimator was used to find sources with a significance $>5\sigma$. A significance map and an excess map were then generated. The significance distribution of the background events was checked to be a standard Gaussian distribution.

3.6 Analysis: Orbital Parameters

3.6.1 Orbit Class

Phase and True Anomaly calculation

The true anomaly is the angle between lines drawn from the centre of mass (near the centre of the stellar companion) to the compact object and to the periastron point, where the compact object comes closest to the star(of Encyclopaedia 2013). This is shown in Figure 3.8.
The PyAstronomy(Czesla et al. 2019) package was used to create a Keplerian ellipse using the orbital parameters given by van Soelen et al. (2019). The true anomaly is

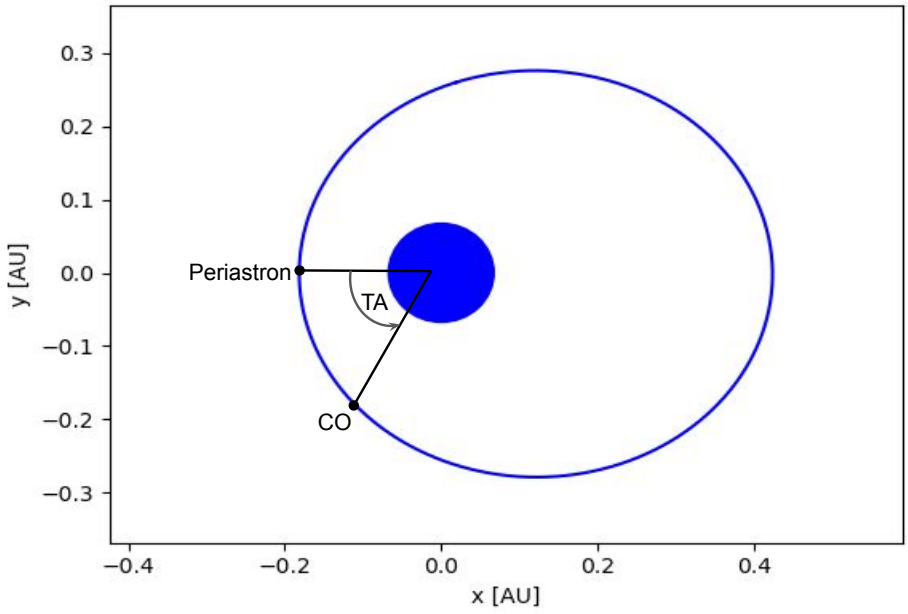


FIGURE 3.8: The true anomaly is the angle, TA, drawn from periastron, through the star and to the current position of the orbiting body, CO.

calculated using the xyzPos(t) function of the KeplerEllipse object that returns the position and true anomaly at any time t.

3.6.2 Orbital binning

The orbital bins were defined in the true anomaly, because this gives the angle between the compact object, the star and the line-of-sight of the observer. The bounds of the inferior and superior conjunction bin are defined where the compact object goes from $-R_*$ to $+R_*$ in the front and back of the star, respectively. The other bins are the same angular size as the conjunction bins ($\sim 34°$), except the periastron bin ($\sim 68°$) and the post-apastron bin ($\sim 80°$). This is shown in Figure 3.9.

3.6.3 Run Sorting

The runs were grouped according to their true anomaly bin, and the energy spectra and flux points were extracted for all the true anomaly bins.

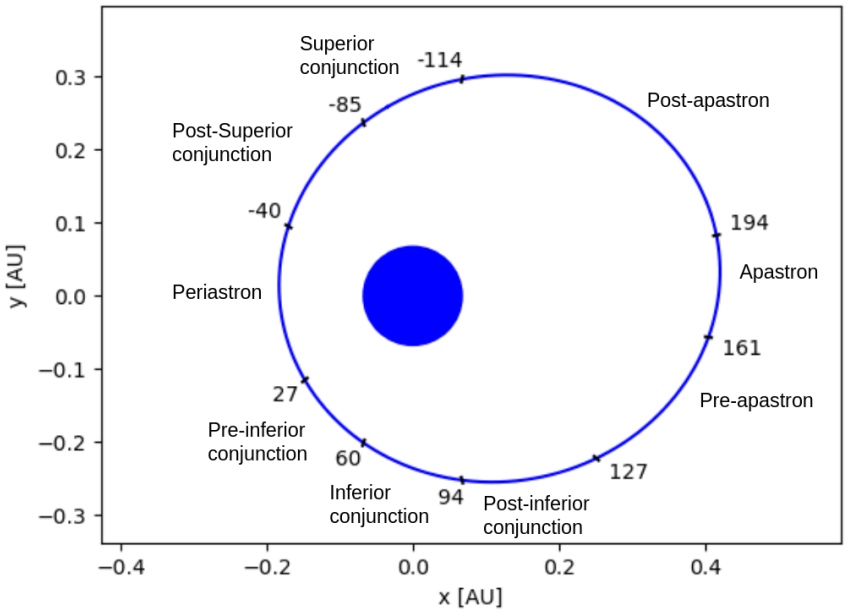


FIGURE 3.9: Orbital binning

3.6.4 Naima Modelling

The python package *naima* was used to model inverse Compton scattering in LMC P3. Inverse Compton scattering depends on the differential cross-section of the electron, which determines the interaction probability with the seed photon. *naima* uses the differential cross-section from Aharonian & Atoyan (1981). The dominant photon field is the stellar radiation from the companion, hence the analytical approximation to IC upscattering of a blackbody from Khangulyan et al. (2014) is used. Since the scattering occurs with multiple electrons, *InverseCompton* function is defined to take in an energy spectrum for the electrons, the seed photon field(s) and the optional parameters of the minimum and maximum energies of the electrons to calculate the flux produced.

Electron Spectrum

The *InverseCompton* function takes in a particle distribution which can be a range of energy spectra. For this study, a power law spectrum of electrons was used. The amplitude is inputted in units of particles per unit of energy with an index of -1.5. The electrons are set to have energies between 0.5 and 50 TeV and a total energy of

5×10^{37} erg. These values are taken from Abdalla et al. (2018), with the total energy reduced by a factor of five to produce a maximum flux similar to the maximum flux found in the on peak phase bin 0.268-0.366.

Seed Photon Field

The centre of mass of the binary system is closer to the stellar companion, so it can be taken that the compact object is in orbit around the stellar companion. It is also assumed that the γ-ray emission region is closer to the compact object. So as the compact object is in orbit around the star, the scattering angle and the density of the photon field change. Hence, the seed photon field inputted is an anisotropic black-body of temperature 39400 K van Soelen et al. (2018) and the luminosity $5.4 \times 10^5 L_\odot$ (Martins et al. 2005). The energy density at a distance of 0.32 AU is 240 erg cm^{-3}. This assumes that we only consider head-on collisions between the electrons from the compact object and the photons from the star. The scattering angle of the detected photons can then be calculated as $\theta = TA - 90^\circ + \omega$ where TA is the true anomaly, and ω is the longitude of periastron. The inclination of the binary system is assumed to be 90°.

Model

Using the seed photon field and electron spectrum outlined above, the spectral energy distribution is calculated at a distance of 50 kpcs for the entire orbit's true anomaly values. The resulting points are plotted against the true anomalies.

Chapter 4

Results

4.1 Sky Maps

The sky maps were produced using LMC P3 as the source region. They were produced using 1344 runs from 8 December 2003 to 7 October 2022. The ring background method was used to extract the background. The ring has a radius of 0.3°and a width of 0.2°. The sky maps that show the full LMC with all source were constructed with a width of 6 °, and the sky maps which show the significance of LMC P3 close up is constructed with a width of 2 °.

All Runs

Significant sources were found using a Gammapy function that finds peaks greater than 5 σ in the significance map. LMC P3 was detected with a significance of 5.6σ. N 157B was detected at a significance of 56σ. N 132D was detected with a significance of 8.1σ. Potential emission was found at (279.55°, -33.34°) with a significance of 5.3σ. A detailed investigation into the orgigin and nature of this emission is beyond the scope of this dissertation. This result is shown in Figure 4.1.

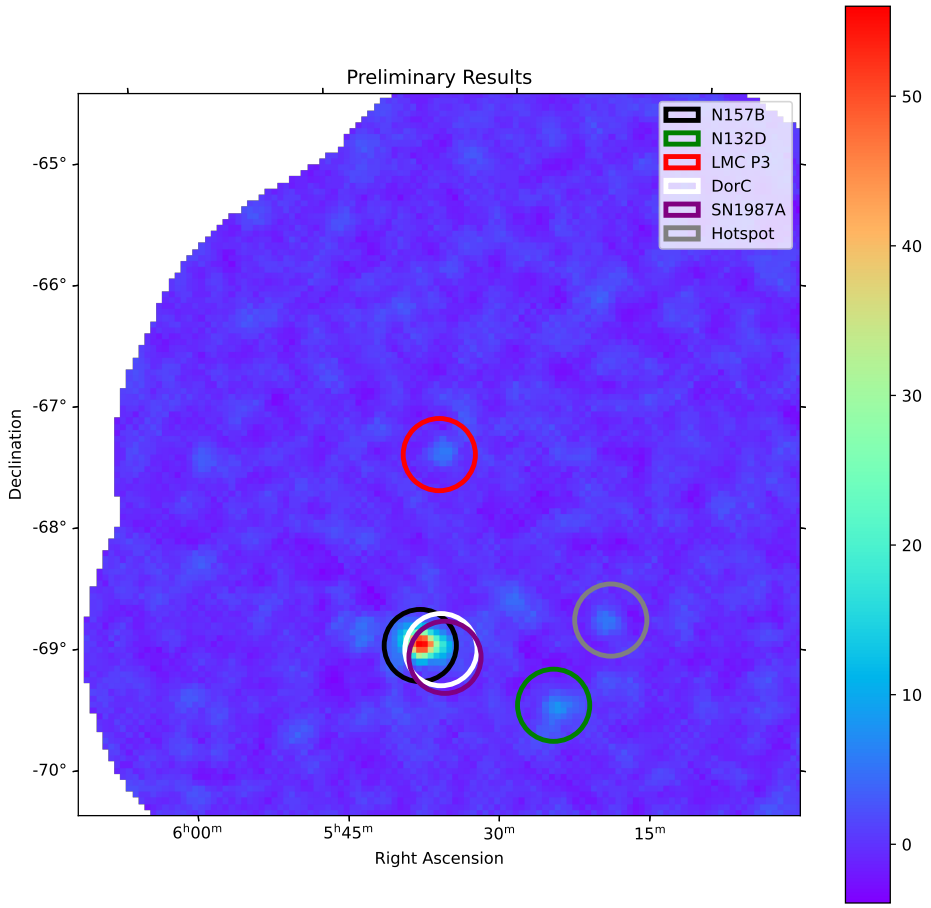


FIGURE 4.1: Significance map of gamma-ray sources in the LMC. A red circle indicates LMC P3, other sources are also indicated. N 157B (black circle), N 132D (green circle), Dor C (white circle), SN 1987A (purple circle) and an unidentified source labelled as 'Hot spot' (grey circle).

Figure 4.2 shows the resulting significance map for LMC P3 in detail, where it is not as outshined by N 157B.

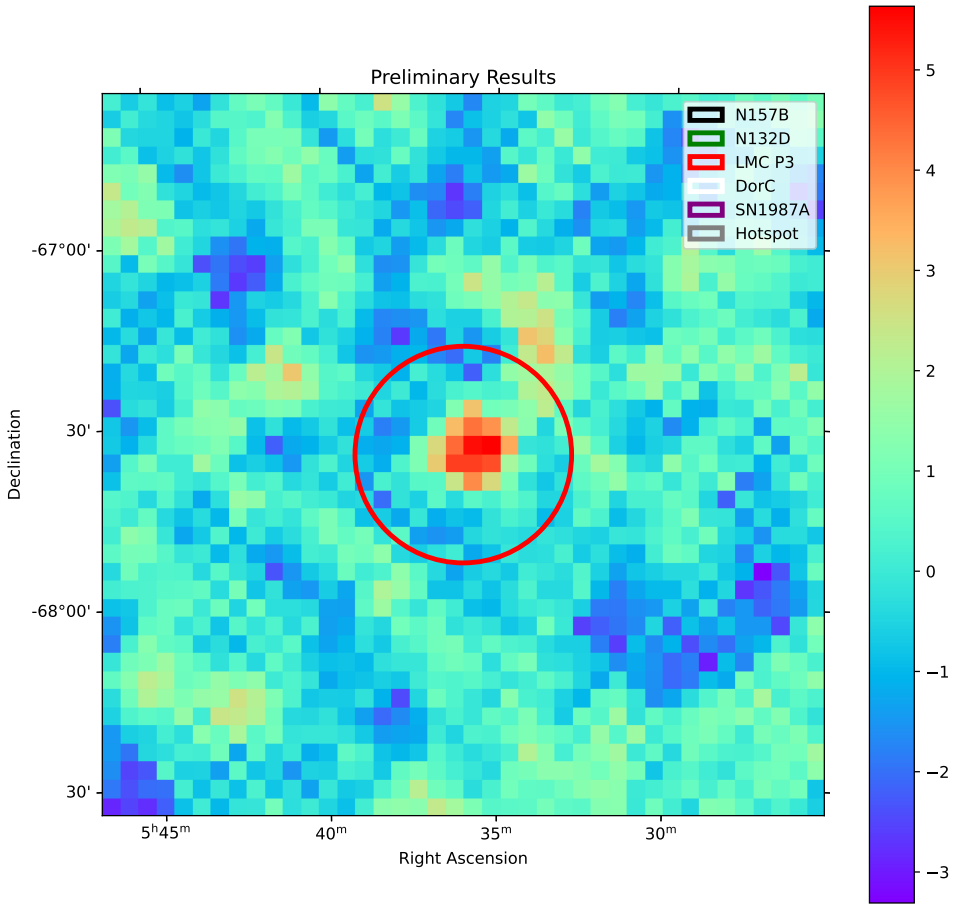


FIGURE 4.2: This figure shows a zoomed-in significance map of LMC P3 (red circle). It was detected at a significance of 5.6σ.

The significance distribution outside the exclusion regions was fit with a standard Gaussian distribution to check that gamma-ray events do not contaminate the background estimation. This can be the case when exclusion regions are not large enough. The Gaussian distribution for all the runs is shown in Figure 4.3. The expectation is to have a Gaussian centred on 0, with a width of 1. The results agree with this,

hence, the exclusion mask is acceptable. The results of this are interpreted in Chapter 5.

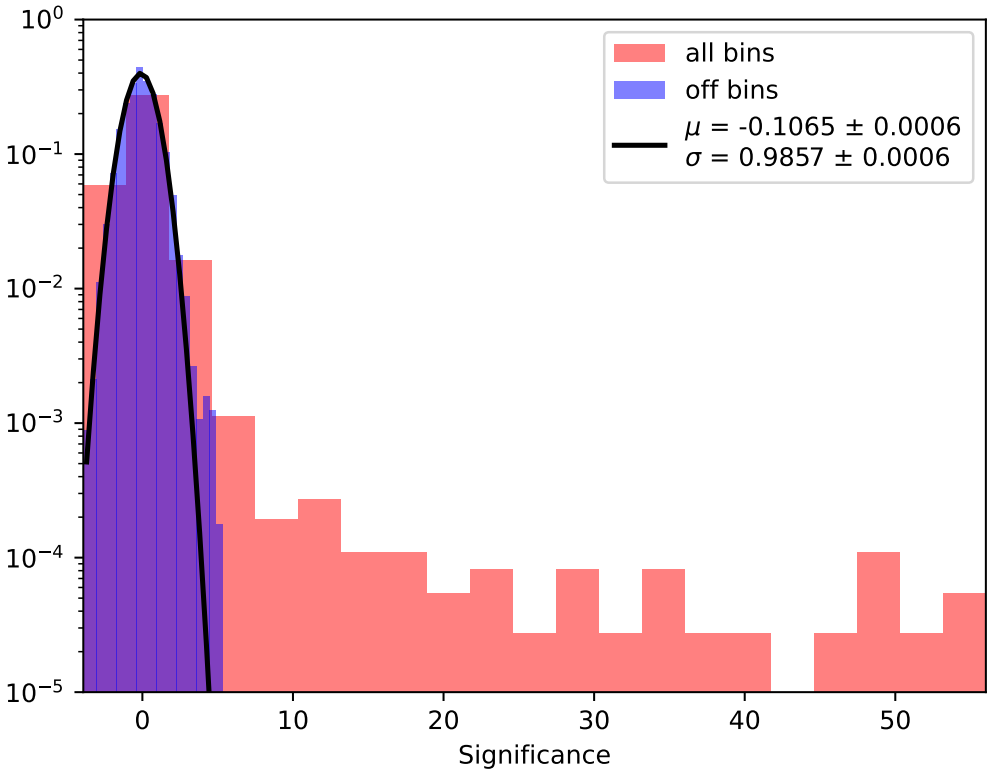


FIGURE 4.3: Gaussian fit of the off-regions. This is the plot for all 1344 runs. Fit result: μ = -0.1065 $\pm$ 0.0006, σ = 0.9857 $\pm$ 0.0006.

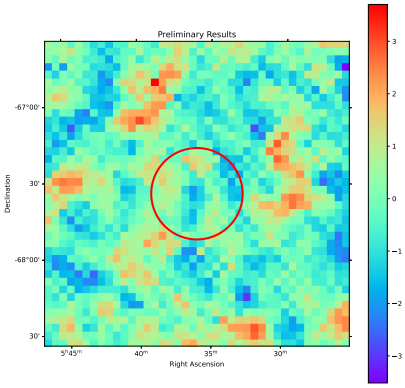
4.1.1 Orbitally resolved Sky Maps

The significance distribution of the background region was also fit to a Gaussian distribution for each phase bin and the result is shown in Table 4.1. Figures 4.4 and 4.5 show the resulting sky maps for each TA bin. Figure 4.4 shows the significance maps from the superior conjunction bin to the bin just before the inferior conjunction. These bins do not show any significant emissions. The significance is around 0 for most of the bins; however, around periastron (0.088-0.164), the emission is around 4σ. Figure 4.5 shows the significance maps for the inferior conjunction bin

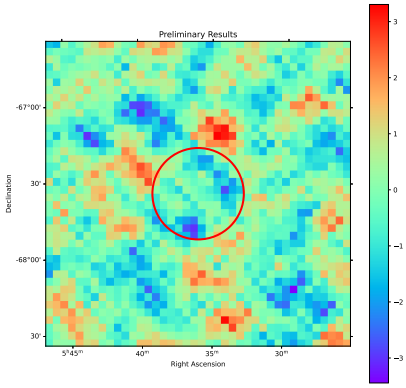
TABLE 4.1: Fit results of the Gaussian off-regions at different orbital phases.

Phase of the orbit	μ	σ
Superior Conjunction (0.946-0.017)	μ = -0.106 $\pm$ 0.002	σ = 1.012 $\pm$ 0.002
Post-superior Conjunction(0.017-0.088)	μ = -0.096 $\pm$ 0.001	σ = 1.021 $\pm$ 0.001
Periastron (0.088-0.164)	μ = -0.0873 $\pm$ 0.0007	σ = 1.0001 $\pm$ 0.0007
Pre-inferior Conjunction (0.164-0.207)	μ = -0.173 $\pm$ 0.004	σ = 1.026 $\pm$ 0.004
Inferior conjunction (0.207-0.268)	μ = -0.054 $\pm$ 0.001	σ = 0.997 $\pm$ 0.001
Post-inferior Conjucntion (0.268-0.366)	μ = -0.113 $\pm$ 0.001	σ = 1.048 $\pm$ 0.001
Pre-apastron (0.366-0.522)	μ = -0.053 $\pm$ 0.001	σ = 0.987 $\pm$ 0.001
Apastron (0.522-0.634)	μ = -0.067 $\pm$ 0.001	σ = 1.023 $\pm$ 0.001
Post-apastron (0.634-0.946)	μ = -0.048 $\pm$ 0.001	σ = 0.959 $\pm$ 0.001

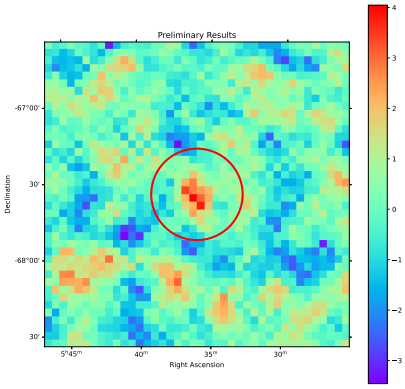
(0.207-0.268) to the bin after apastron (0.634-0.946). The bin with a firm detection is the Post-inferior Conjunction bin (0.268-0.366), detected with a significance of 8σ. The inferior conjunction bin shows a significance of around 4σ.



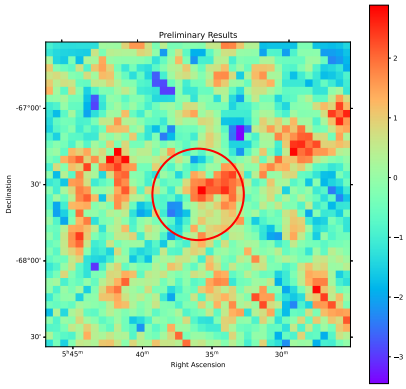
(a) Superior Conjunction (0.946-0.017)



(b) Post-superior Conjunction (0.017-0.088)

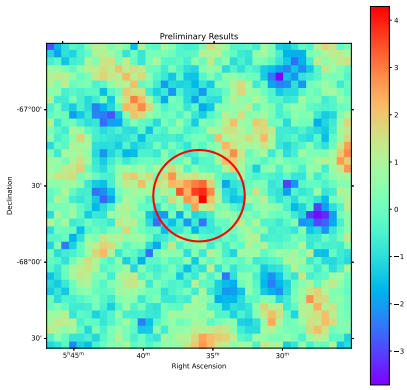


(c) Periastron (0.088-0.164)

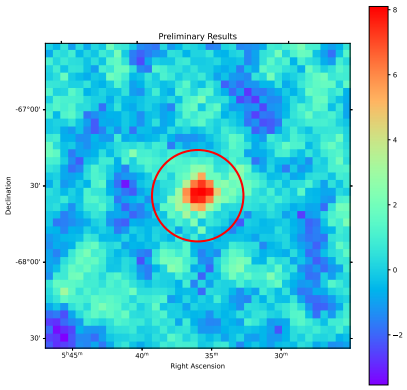


(d) Pre-Inferior Conjunction (0.164-0.207)

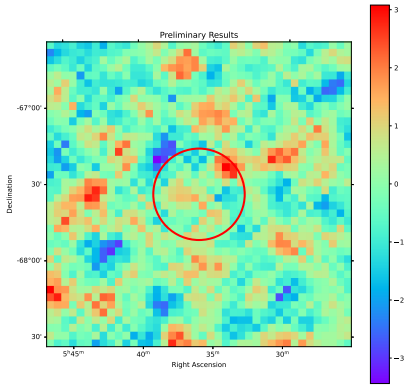
FIGURE 4.4: Significance maps at different orbital phases. This figure shows significance maps from the superior conjunction through the periastron bin (0.088-0.164) to the bin before the inferior conjunction (0.164-0.207) of the system. All the bins show a significance $<3\sigma$ for LMC P3, except the bin at periastron (0.088-0.164), which shows a significance of around 4σ.



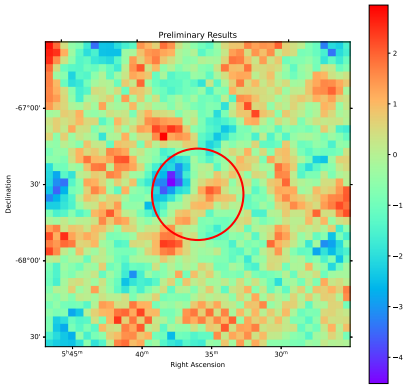
(e) Inferior Conjunction (0.207-0.268)



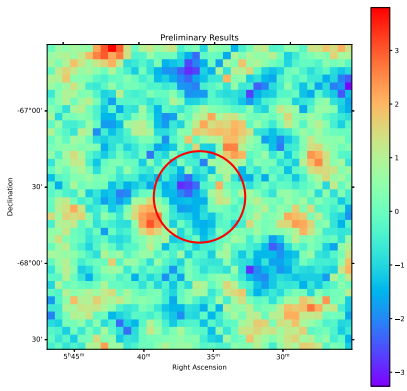
(f) Post-Inferior Conjunction (0.268-0.366)



(g) Pre-apastron (0.366-0.522)



(h) Apastron (0.522-0.634)



(i) Post-apastron (0.634-0.946)

FIGURE 4.5: Significance maps at different orbital phases. This figure shows the significance maps though inferior conjunction (0.207-0.268) to after apastron (0.522-0.634). The only bin which shows a significant detection of 8σ is the post-inferior conjunction bin (0.268-0.366).

4.2 Spectral Results

4.2.1 Background Determination

The background for the spectra are determined by the Reflected Regions background method(Berge et al. 2007). The background regions are determined by using multiple off regions. The off regions are selected around the source, excluding regions that have a significance of $\geq 5\sigma$ or could potentially have gamma-ray emission that has not been detected yet, such as SN1987A. This is shown in Figure 4.6.

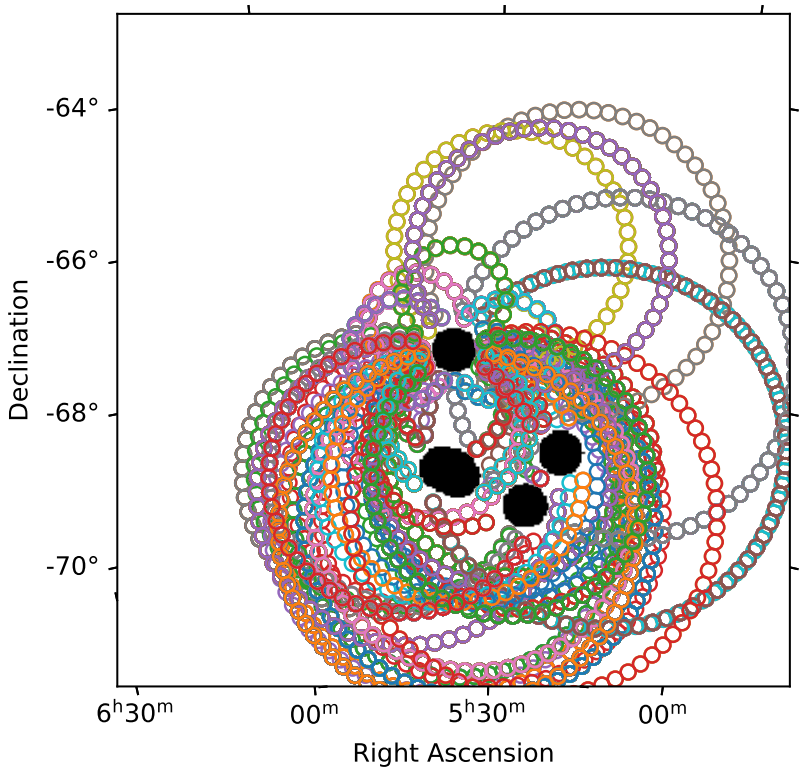


FIGURE 4.6: Background determination of LMC P3. The coloured circles show the background regions selected. The blacked out regions show the areas on the map which have not been used to determine the background, to prevent the background estimation from being contaminated by source emission.

4.2.2 N 157B Consistency Check

Data

Several configurations were tested to determine which H.E.S.S. Configuration results in the best N 157B spectrum reproduction. The number of runs is 1281 (∼502.7 hours livetime) for all the configurations except H.E.S.S. II Stereo Standard, which has 203 runs (∼72.6 hours livetime). The H.E.S.S. II Stereo Standard data set runs from 6 November 2013 to 30 September 2019. The other data sets consist of observations from 18 December 2003 to 7 October 2022.

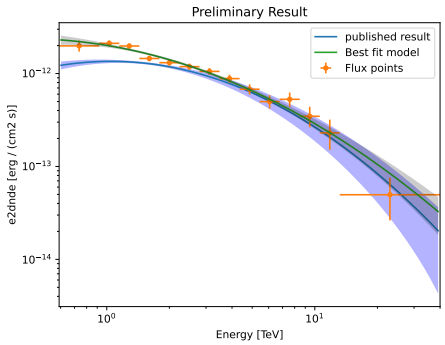
Log Parabola Parameters

The log parabola spectral fits for different configurations are listed in Table 4.2, and the plots for these compared to the published results are shown in Figure 4.7. The disagreement between the published results and these spectra is discussed in Chapter 5. The analysis configuration which shows the most agreement with the published spectrum is H.E.S.S. I Stereo Faint. This is shown in Figure 4.8. This spectrum is plotted with the calculated flux points. The differential energy spectrum is determined from the ∼502.7 hr of observations conducted from 2003 to 2022. A log parabola fit yields:

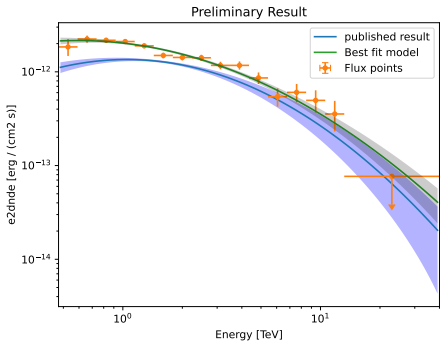
$$\frac{dN}{dE} = (4.6 \pm 0.1) \times 10^{-9}\mathrm{m}^{-2}\mathrm{s}^{-1}\mathrm{TeV}^{-1} \left(\frac{E}{1.5\mathrm{TeV}}\right)^{-(2.54\pm0.08)-(0.21\pm0.06)\times\ln\left(\frac{E}{1.5\mathrm{TeV}}\right)}$$

TABLE 4.2: Log Parabola Parameters for N157B. The analysis configuration, published result(Komin et al. 2020), spectral parameters, luminosity between 1-10 TeV and the significance of the log parabola fit being better than the power law fit is shown.

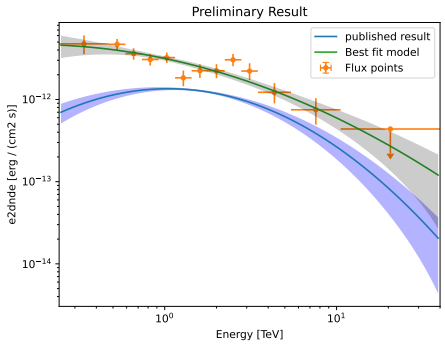
Configuration	Φ_0	α	β	**Luminosity**	σ **Preferred**
	$\times 10^{-9}$ $(\mathrm{m^2 s TeV})^{-1}$			$(\times 10^{35} \mathrm{erg/s})$	
Published Result	3.6 ± 0.1	2.23 ± 0.08	0.32 ± 0.07	6.5 ± 0.3	4.4σ
H.E.S.S. I Stereo Faint	4.6 ± 0.1	2.54 ± 0.08	0.21 ± 0.06	7.9 ± 0.2	3.92σ
H.E.S.S. I Stereo Standard	4.9 ± 0.1	2.58 ± 0.03	0.23 ± 0.04	8.6 ± 0.2	5.97σ
H.E.S.S. II Stereo Standard	7.2 ± 0.5	2.54 ± 0.9	0.12 ± 0.08	12.6 ± 0.9	1.7σ
H.E.S.S. I Stereo Loose	5.1 ± 0.1	2.41 ± 0.04	0.22 ± 0.04	8.8 ± 0.2	6.4σ
H.E.S.S. I Stereo Very Loose	5.2 ± 0.2	2.43 ± 0.04	0.19 ± 0.04	9.1 ± 0.3	6.22σ



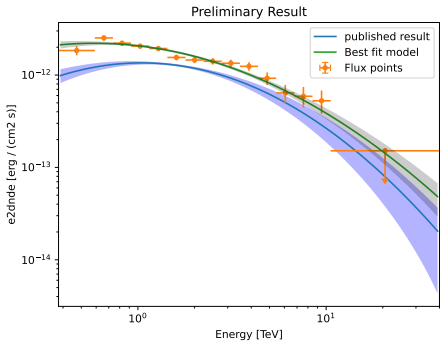
(a) H.E.S.S. I Stereo Faint



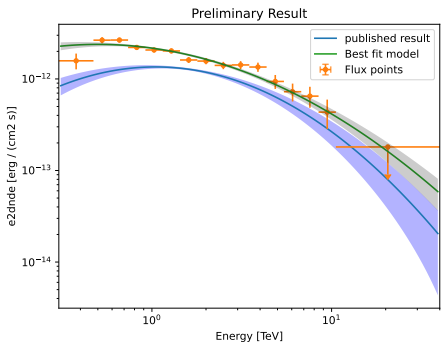
(b) H.E.S.S. I Stereo Standard



(c) H.E.S.S. II Stereo Standard



(d) H.E.S.S. I Stereo Loose



(e) H.E.S.S. I Stereo Very Loose

FIGURE 4.7: The comparison of various log parabola fits for different H.E.S.S. analysis configurations (orange lines) compared to the published spectrum(blue line). It can be seen that the amplitudes for the various fits are higher than the published amplitude.

Figure 4.8 shows the published spectrum and this analysis result using the H.E.S.S. I Stereo Faint configuration.

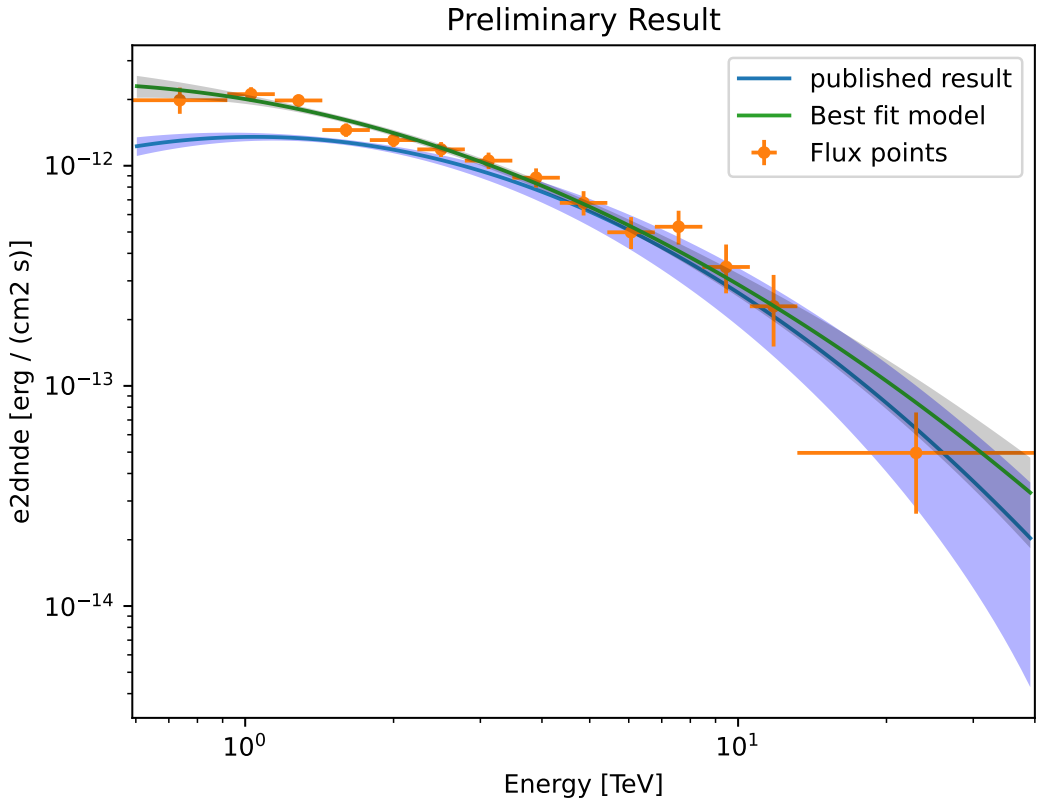


FIGURE 4.8: The published H.E.S.S. spectrum (Blue line) is plotted with the result obtained from this analysis (Orange line). This result is obtained by stacking the runs using the H.E.S.S. I Stereo Faint configuration.

Flux Estimates

The flux points for the spectrum of N 157B were estimated using a binning that ensures that each flux point has a significance of at least 2σ. The result can be seen in Figure 4.9.

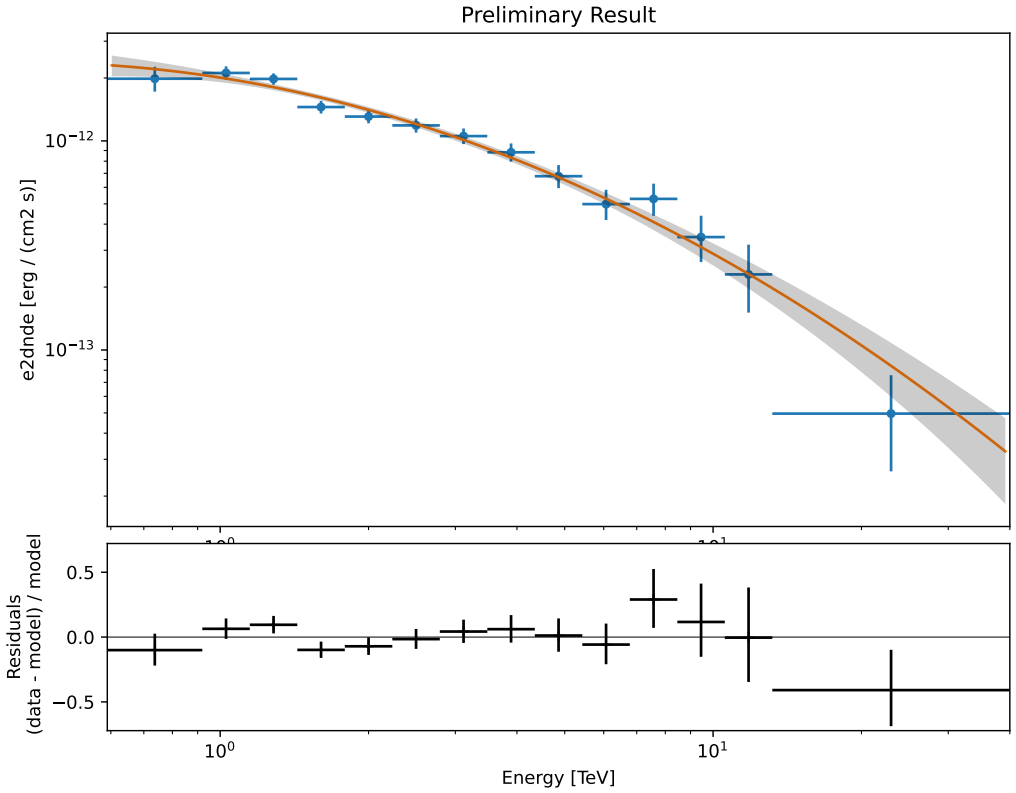


FIGURE 4.9: The log parabola differential energy spectrum for N 157B. The spectral binning is optimised such that each flux point has a significance of at least 2σ.

The runs of N 157B were folded on the orbital period of LMC P3. This is because N 157B is the brightest source in the LMC and is not known to be a variable source (Komin et al. 2020) and to check that the variability in LMC P3 is intrinsic and not due to systematic effects or the differences between Gammapy and the standard H.E.S.S. analysis pipeline. The flux estimate for all the runs of N 157B was

$$F(1-10\text{TeV}) = (8.9 \pm 0.2) \times 10^{-9}\text{m}^{-2}\text{s}^{-1}$$

Fit with a constant defined by $y = (8.9 \times 10^{-9}) \times a\ \text{m}^{-2}\text{s}^{-1}$ The fit gives the parameter, a, a value of 1.00 ± 0.03.

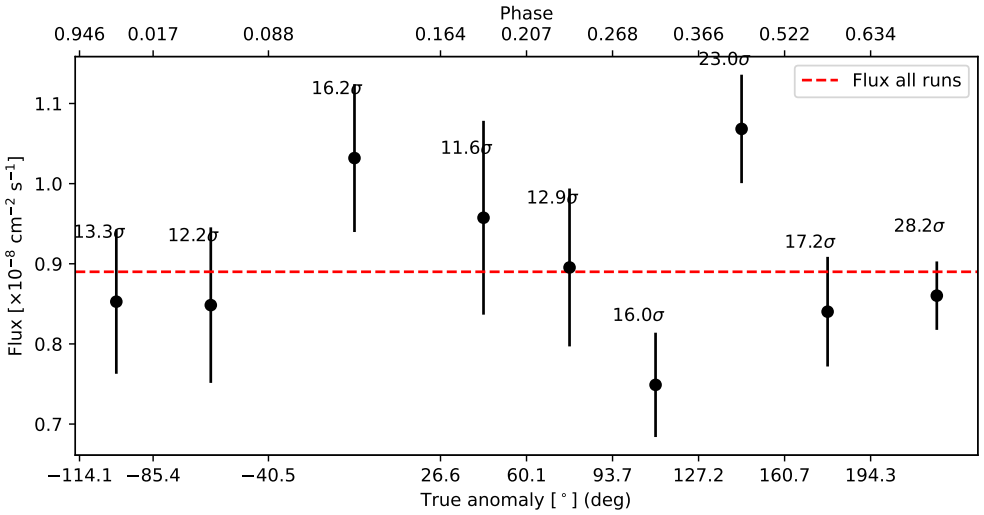


FIGURE 4.10: The runs for N 157B folded on the period of LMC P3 to check if the flux is constant.

TABLE 4.3: Data sets for LMC P3. The phase is defined with 0 at the maximum of the GeV emission as used by Corbet et al. (2016). The heterogeneous phase bins were found by splitting the orbit as described in Section 3.6. Sigma is the significance found in the entire energy range detectable by H.E.S.S. The Excess is the number of counts after the background gamma-ray counts were subtracted. Livetime describes the total on-region time, and Runs are the number of observations.

Phase of the orbit	**Phase Bin**	**Significance**	**Excess**	**Livetime (h)**	**Runs**
Full Orbit	0.0 - 1.0	5.0σ	91.78	371.8	1344
Superior Conjunction	0.946 - 0.017	-0.9σ	-4.08	24.2	95
Post-superior Conjunction	0.017 - 0.088	0.4σ	1.60	20.8	80
Periastron	0.088 - 0.164	1.3σ	7.075	30.2	109
Pre-inferior Conjunction	0.164 - 0.207	3.1σ	9.11	9.7	51
Inferior Conjunction	0.207 - 0.268	4.7σ	28.19	27.6	93
Post-inferior Conjunction	0.268 - 0.366	7.8σ	60.73	43.6	146
Pre-apastron	0.366 - 0.522	1.4σ	9.69	58.0	206
Apastron	0.522 - 0.634	-0.7σ	-4.16	44.7	156
Post-apastron	0.634 - 0.964	-1.9σ	-16.37	113.0	408

4.2.3 LMC P3

Data

The data set for LMC P3 consists of 1344 runs (~371.8 hr livetime) taken between 18 December 2003 to 7 October 2022. The 1344 runs were sorted according to their orbital phase described in Section 3.6. A detailed breakdown of the resulting datasets is given in Table 4.3.

Figure 4.11 shows the relationship between the significance, excess counts and livetime and their evolution across phase bins. Although the orbital bin size and thus the number of runs (livetime) in each bin varies, there is a clear increase and decrease in excess and significance around the emission peak after inferior conjunction (0.268-0.366). It is interesting to note how significantly the emission dips below a significantly detectable level. The only phase bin with emission above 5 σ is the Post-inferior conjunction bin (0.268-0.366).

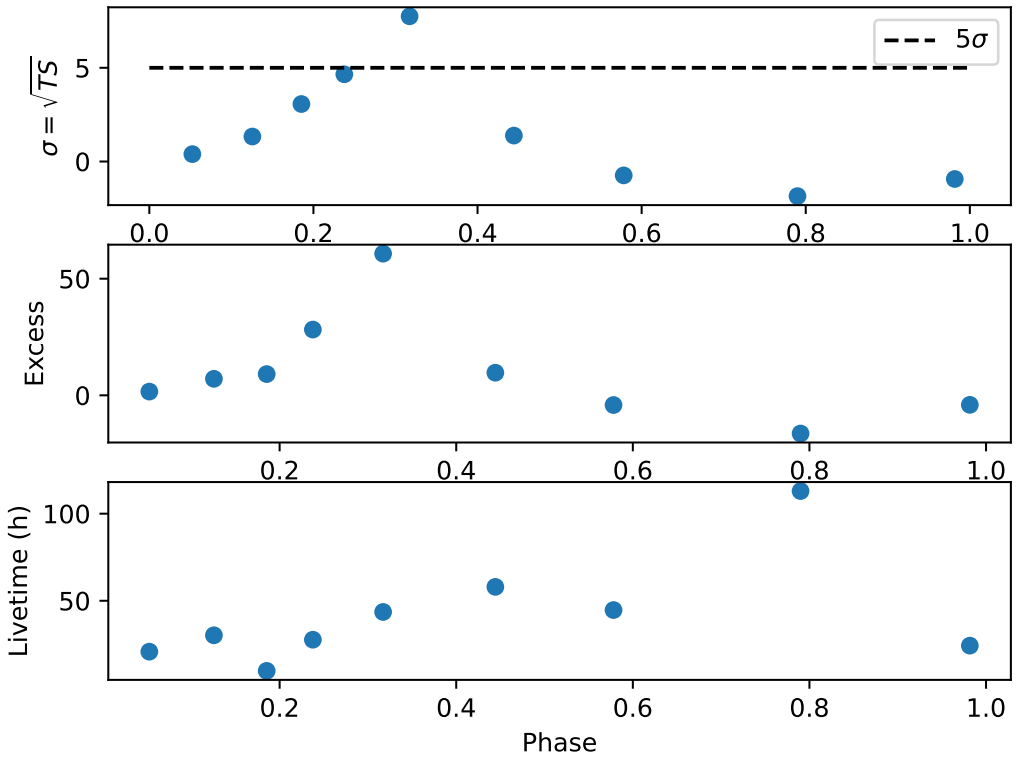


FIGURE 4.11: Significance evolution for LMC P3. The total significance (Top Panel) for different orbital phases of LMC P3 as well as the excess (Middle Panel) and live-time (Bottom Panel), are plotted for LMC P3. A black dashed line in the top panel indicates the 5σ significance level.

Power Law parameters

The power law spectral fits for different orbital phases are listed in Table 4.4.
The differential energy spectrum is determined from the ~371.8 hr of observations conducted from 2003 to 2022. A power law fit yields:

$$\left(\frac{dN}{dE}\right)_{FullOrbit} = (1.3 \pm 0.4) \times 10^{-9} \mathrm{m}^{-2}\mathrm{s}^{-1}\mathrm{TeV}^{-1} \left(\frac{E}{1\mathrm{TeV}}\right)^{-(2.4\pm0.3)}$$

Figure 4.12 shows the orbital averaged spectrum with the estimated flux points, which are found in Table 4.5.

TABLE 4.4: Power law Parameters for LMC P3. The power law fit is only calculated for phases with at least a 3σ total significance. The spectral index was fixed to 2.4 for bins without detections, the value found for the full orbit, so flux estimates can be obtained. The luminosity upper limits are calculated at the 95 % significance level.

Phase of the orbit	$\Phi_0(\times 10^{-9}\mathbf{m}^{-2}\mathbf{s}^{-1}\mathbf{TeV}^{-1})$	Γ	**Luminosity**$(\times 10^{35}\mathbf{erg/s})$
Full Orbit	1.3 ± 0.4	2.4 ± 0.3	0.9 ± 0.2
Superior Conjunction (0.946-0.017)	-	2.4 fixed	< 0.41
Post-superior Conjunction (0.017-0.088)	-	2.4 fixed	< 1.6
Periastron (0.088-0.164)	-	2.4 fixed	< 2.2
Pre-inferior Conjunction (0.164-0.207)	7 ± 5	3 ± 1	3 ± 1
Inferior Conjunction (0.207-0.268)	4 ± 2	2.3 ± 0.4	3.1 ± 0.8
Post-inferior Conjunction (0.268-0.366)	5 ± 1	2.2 ± 0.2	4.8 ± 0.8
Pre-apastron (0.366-0.522)	-	2.4 fixed	< 1.52
Apastron (0.522-0.634)	-	2.4 fixed	< 0.077
Post-apastron (0.634-0.946)	-	2.4 fixed	< 0.10

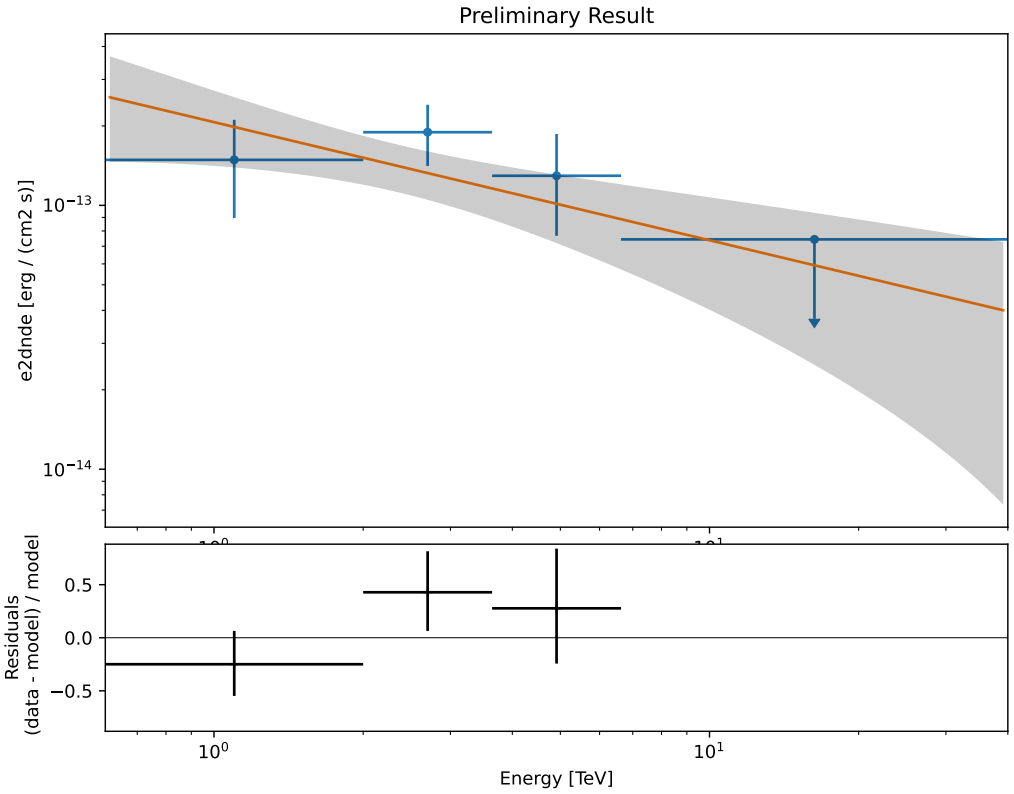


FIGURE 4.12: The power law differential energy spectrum for LMC P3. This result includes all the runs for LMC P3. Upper limits were determined at the 95% confidence interval.

TABLE 4.5: SED points used to plot Figure 4.12.

E_{ref}	E_{min}	E_{max}	$E^2\frac{dN}{dE}$	$\Delta\left(E^2\frac{dN}{dE}\right)$	$E^2\frac{dN}{dE}_{ul}$	**Significance**
erg	erg	erg	erg s^{-1} cm^{-2}	erg s^{-1} cm^{-2}	erg s^{-1} cm^{-2}	
			10^{-13}	10^{-13}	10^{-13}	
1.8	1.0	3.2	1.5	0.6	<2.8	2.6
4.3	3.2	5.8	1.9	0.5	<2.9	4.3
7.9	5.8	10.6	1.3	0.5	<2.5	2.6
26.1	10.6	64.1	-	-	<0.7	-0.20

The power law fit for the on-peak region (Post-inferior conjunction, 0.268-0.366) yields:

$$\left(\frac{dN}{dE}\right)_{Post-INF} = (5 \pm 1) \times 10^{-9}\mathrm{m}^{-2}\mathrm{s}^{-1}\mathrm{TeV}^{-1}\left(\frac{E}{1\mathrm{TeV}}\right)^{-(2.2\pm0.2)}$$

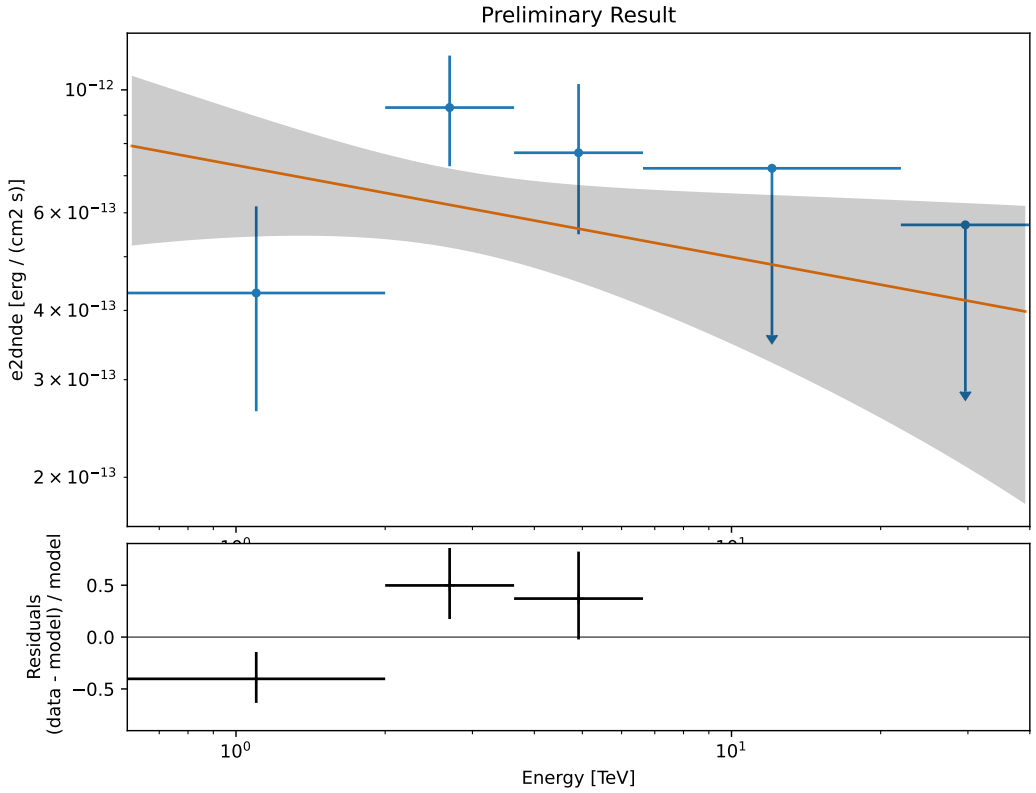


FIGURE 4.13: The power law differential energy spectrum for LMC P3 after inferior conjunction (0.268-0.366). This result includes runs for LMC P3 that occur in the true anomaly range 94°to 127°, which places the emission peak after inferior conjunction (0.268-0.366). Upper limits were determined at the 95% confidence interval.

Flux Estimates

The gamma-ray flux at different phases were calculated between 1-10 TeV. For bins where the significance in this energy range is lower than 3σ, upper limits on the flux is calculated at the 95% confidence level. The flux points are tabulated in Table 4.6 The peak of emission is seen after inferior conjunction (0.268-0.366).

TABLE 4.6: Flux estimates for LMC P3. The significance shown is for the flux points calculated in the 1-10 TeV energy range. Upper limits are calculated at the 95% confidence range.

Phase of the orbit	**Significance**	**Flux** $\times 10^{-13}$ cm $^{-2}$ s^{-1}	**Upper Limit** $\times 10^{-13}$ cm $^{-2}$ s^{-1}
Full Orbit	5.2σ	0.8 ± 0.2	<1.10
Superior Conjunction (0.946-0.017)	-1.4σ	-	<0.36
Post-superior Conjunction (0.017-0.088)	0.0σ	-	<1.38
Periastron (0.088-0.164)	1.7σ	-	<1.92
Pre-inferior Conjunction (0.164-0.207)	3.0σ	3 ± 1	<5.57
Inferior Conjunction (0.207-0.268)	4.7σ	2.5 ± 0.7	<4.02
Post-inferior Conjunction (0.268-0.366)	8.3σ	3.7 ± 0.6	<4.95
Pre-apastron (0.366-0.522)	1.2σ	-	<1.32
Apastron (0.522-0.634)	-0.5σ	-	<0.678
Post-apastron (0.634-0.946)	-1.7σ	-	<0.09

4.2.4 Orbital Binning

Phase-resolved Energy Spectrum

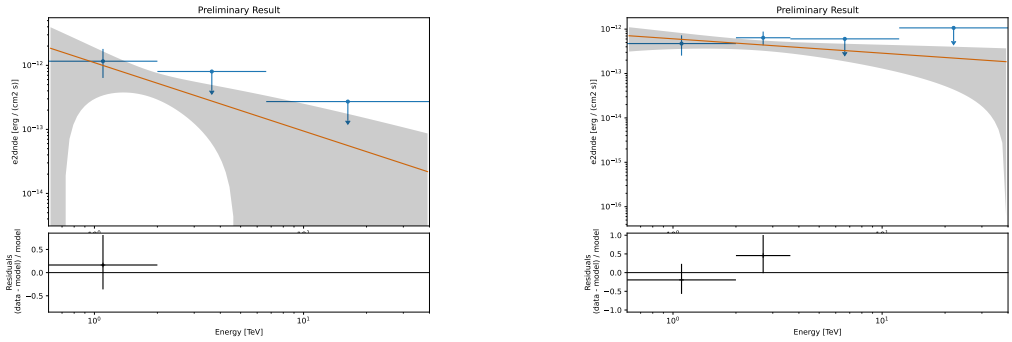
The spectrum for different phase bins above 3σ is determined, and the rest are set to the fit result of the full orbit spectral index. This is shown in Figure 4.13 and 4.14. The corresponding SED points are shown in Tables 4.7 (before inferior conjunction, 0.164-0.207), 4.8 (inferior conjunction, 0.207-0.268), and 4.9 (after inferior conjunction, 0.268-0.366).

TABLE 4.7: SED points used to plot the Pre-inferior conjunction bin (0.164-0.207) spectrum in Figure 4.14.

E_{ref}	E_{min}	E_{max}	$E^2\frac{dN}{dE}$	$\Delta\left(E^2\frac{dN}{dE}\right)$	$E^2\frac{dN}{dE}_{ul}$	**Significance**
erg	erg	erg	erg s^{-1} cm^{-2}	erg s^{-1} cm^{-2}	erg s^{-1} cm^{-2}	
			10^{-13}	10^{-13}	10^{-13}	
1.8	1.0	3.2	11	6	<25.8	2.7
5.8	3.2	10.6	-	-	<8.0	2.0
26.1	10.6	64.1	-	-	<2.7	-1.0

TABLE 4.8: SED points used to plot the inferior conjunction (0.207-0.268) spectrum in Figure 4.14.

E_{ref}	E_{min}	E_{max}	$E^2\frac{dN}{dE}$	$\Delta\left(E^2\frac{dN}{dE}\right)$	$E^2\frac{dN}{dE}_{ul}$	**Significance**
erg	erg	erg	erg s^{-1} cm^{-2}	erg s^{-1} cm^{-2}	erg s^{-1} cm^{-2}	
			10^{-13}	10^{-13}	10^{-13}	
1.8	1.0	3.2	5	2	<10.1	2.4
4.3	3.2	5.8	6	2	<11.6	3.9
10.6	5.8	19.3	-	-	<6.0	1.6
35.2	19.3	64.1	-	-	<10.7	1.2



(a) Pre-Inferior Conjunction (0.164-0.207) (b) Inferior Conjunction (0.207-0.268)

FIGURE 4.14: The power law differential energy spectrum for LMC P3 at different points in the orbit. Upper limits were determined at the 95% confidence interval.

TABLE 4.9: SED points used to plot Figure 4.13.

E_{ref}	E_{min}	E_{max}	$E^2 \frac{dN}{dE}$	$\Delta\left(E^2 \frac{dN}{dE}\right)$	$E^2 \frac{dN}{dE}_{ul}$	**Significance**
erg	erg	erg	erg s^{-1} cm^{-2}	erg s^{-1} cm^{-2}	erg s^{-1} cm^{-2}	
			10^{-13}	10^{-13}	10^{-13}	
1.8	1.0	3.2	4	2	<8.2	2.9
4.3	3.2	5.8	9	2	<14.0	6.3
7.9	5.8	10.6	8	2	<13.1	4.5
19.3	10.6	35.2	-	-	<7.2	1.9
47.5	35.2	64.1	-	-	<5.7	-0.8

4.2.5 Light Curve

The phase folded light-curve is shown in Figure 4.15. The orbit was broken down into nine phase bins in anticipation of finding emissions in multiple parts of the orbit. However, only one phase bin shows emission above 5σ. Interpreted with the current set of orbital parameters, the peak of the emission occurs after inferior conjunction (0.268-0.366). This phase bin shows the brightest emission and the most significant flux detection. The emission drops sharply after this bin, as the stellar photon diminishes as the compact object moves toward the apastron. Upper limits for phase bins with less than 3σ are shown.

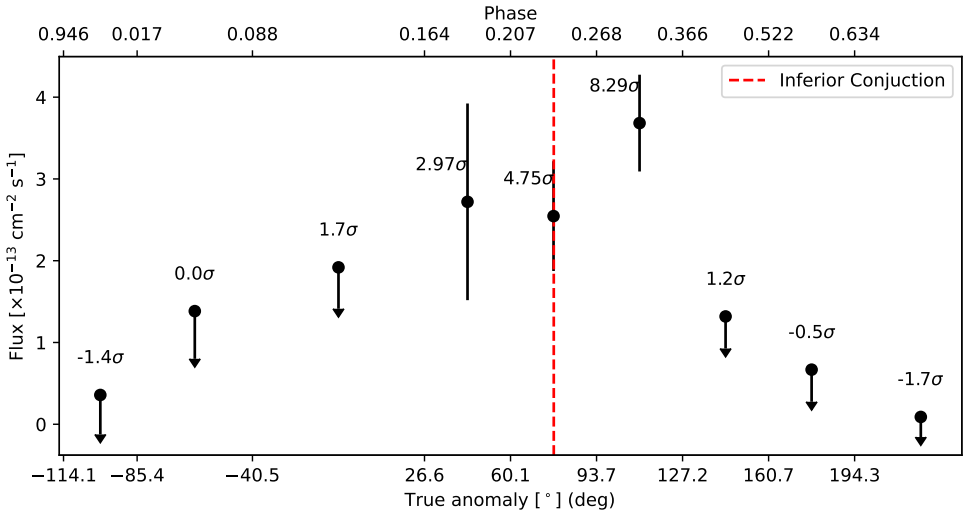


FIGURE 4.15: Lightcurve for LMC P3. The peak flux is observed after inferior conjunction (0.268-0.366) with a significance of 8.29σ. Upper limits are calculated at the 95 % confidence range.

4.3 Naima Modelling

The inverse Compton-modelled light curve is plotted in Figure 4.16. IC scattering depends on the collision angle between the photon and the electron or positron. For a circular orbit, (assuming $i = 90°$) one expects to see the maximum IC flux at superior conjunction, where the collision between the stellar photons and the electron/positron is head-on, and the minimum at inferior conjunction, where tail-on collisions occur. The IC flux also depends on the density of the photon field; this shifts the peak to periastron for elongated (eccentric) orbits, where the photon field is densest. The model takes angular and distance dependence into account. The IC model does not predict the peak in the correct position, which indicates a more extensive model needs to be considered. This will be discussed in Chapter 5.

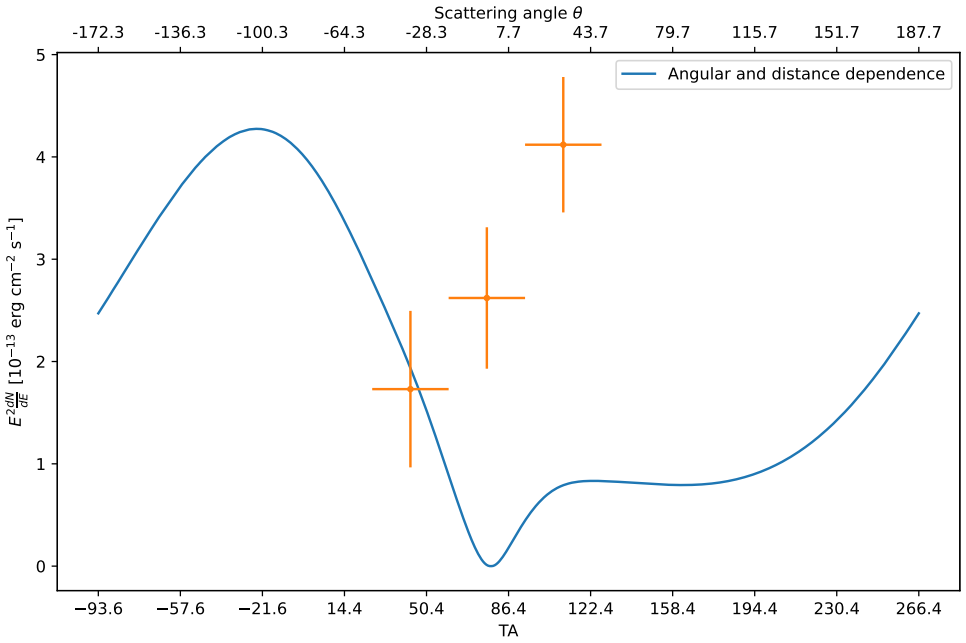


FIGURE 4.16: Inverse Compton Scattering Model for LMC P3 (blue line) and the spectral energy points found from the analysis (orange line). These points consider photons of energy 1 to 10 TeV The top axis shows the scattering angle between the stellar photons and the electrons/positrons from the compact object.

Chapter 5

Discussion

5.1 Research Aims and Objectives

This study aims to produce a temporal and spectral analysis of the gamma-ray binary LMC P3 with the updated H.E.S.S. dataset and orbital parameters. This research aimed to find at which phase of the orbit the peak of the TeV emission is and obtain a light curve with more resolved orbital binning. Ultimately, it is to resolve the TeV light curve. Finding the position of the peak emission is essential because this indicates the physical processes at play in the system. The objective of gathering information on the physics in this system is to fit the light curve to physical models. N 157B is used as a standard candle in the analysis, and the objective is to reproduce the published spectrum of this source and check that we see a constant flux from this system.

5.2 Key Findings

The analysis identifies the peak emission at phase bin 0.268 - 0.366. In terms of the orbital parameters given in van Soelen et al. (2019), this places the peak after inferior conjunction. In terms of true anomaly, it is between 94°and 127°. Therefore, this phase bin is the only one that shows significant emissions above 5σ. The LMC P3 spectrum for all the runs were found to agree with the published spectrum from Abdalla et al. (2018), with an index of 2.4 ± 0.3 and an amplitude of $(1.3 \pm 0.4) \times 10^{-9}\mathrm{m}^{-2}\mathrm{s}^{-1}\mathrm{TeV}^{-1}$. Spectra were found for three phase bins (before inferior conjunction, inferior conjunction and after inferior conjunction) shown in

Figure 4.4. The spectrum of N 157B is reasonably reproduced, and the flux shows slight variation.

5.3 Consistency Check

5.3.1 Spectral Analysis: N 157B

N 157B is the brightest TeV gamma-ray source in the LMC and was used to check the consistency of the analysis. It was found that the H.E.S.S. I Stereo Faint configuration (see Figure 4.8) agrees best with the published results. Below 3 TeV, the energy spectrum from this analysis is higher than the published result, but there is a better agreement above this range. The difference in the lower energies might be due to the differences in the gammapy pipeline and the standard H.E.S.S. Paris Analysis. The differences in the spectral results can also be seen in the luminosity measurements in Tables 4.2. The chosen configuration, H.E.S.S. I Stereo Faint, is the closest to the published value. However, the measured value for the luminosity using the log parabola energy spectrum is 21.5 % higher than the published value (Komin et al. 2020). The power law luminosity is higher by 17.6 %. For the other configurations, the luminosity difference is even greater. The differences in luminosity can be attributed to the increased flux computed at lower energies, shown in the spectrum plots 4.8 and 4.7.

5.3.2 Testing for constant flux

While the flux of N 157B is higher than previously reported, the constant flux fit of

$$F(1-10\mathrm{TeV}) = (8.9 \pm 0.2) \times 10^{-9}\mathrm{m}^{-2}\mathrm{s}^{-1}$$

agreed within a 3% error between the subsets of the data. The error can be due to systematics; the flux points were folded on data from 2003 to 2022. The H.E.S.S. array has undergone multiple changes (e.g. camera upgrades) during this epoch, which may contribute to variation in the flux points determined in these subsets. In addition, the subsets were folded on the same orbital bins of LMC P3, which introduces heterogeneous data sets in terms of size and epochs when the data are

taken. Considering this, and the fact that the dataset is different from the dataset used in the previous publication, the error can also be due to statistical fluctuations.

5.4 Sky Maps

The sky maps were used as a visual representation of the data. N 157B was detected in all the orbital subsets of the data and the full orbit sky map. By fitting the background region with a Gaussian, it has been shown that there are no background sources. An unidentified source was found in the sky maps and added to the exclusion map regions to prevent background contamination with source counts. The Gaussian fits of the background regions are reasonable. Ideally, the standard deviation, σ, should be 1 and the mean, μ, should be 0. The values for the full orbit are shown in Figure 4.3, and the values for the different orbital phases are shown in Table 4.1 all are around 1 and 0, respectively, indicating that there is limited background contamination.

5.5 Spectral Analysis: LMC P3

The Full orbit shows a power law index of 2.4 ± 0.3. This result is consistent with the published 2.5 ± 0.2 (Abdalla et al. 2018). This agreement is surprising since it would be expected to vary more since the updated data set samples the orbit differently than the previously published data. This difference can, however, be seen in the amplitude; it is lower than the published result. The bin with the highest flux and significance has a steeper spectrum than the overall spectrum, with an index of 2.2 ± 0.2 and an amplitude of $(5 \pm 1)^{-9}\mathrm{m}^{-2}\mathrm{s}^{-1}\mathrm{Tev}^{-1}$ which matches the on peak spectrum given in Abdalla et al. (2018)(and given in Table 3.3).

5.6 Temporal Analysis

5.6.1 Light Curve

The light curve shows significant emission in a sharp narrow peak after inferior conjunction.

The peak emission was found to occur at phase bin 0.268 - 0.366, corresponding to true anomaly 94°-127°. The light curve is plotted against true anomalies to infer physical meaning easily. The peak flux, shown in Figure 4.15, is a very narrow peak and comprises only 9.8% of the orbit. The flux is very bright compared to the rest of the orbit with a flux of $(3.7 \pm 0.6)^{-13}$ cm $^{-2}$ s $^{-1}$ between 1 - 10 TeV. Compared to the flux detected in the inferior conjunction, this is a 48 % increase. In addition, it is the only part of the orbit that shows emission above 5σ significance. The emission from the complete orbit, seen in Figure 4.11, also shows a significant detection above 5 σ. Most detectable emissions may be due to the narrow peak after the inferior conjunction. The resolved light curve can help model the system's physical processes.
Figure 4.11 also shows the solid orbital modulation of the emission of the system. The significance and excess counts increase before the Post-inferior conjunction bin and sharply drop as the compact object approaches the apastron.
The emission being strongly tied to orbit indicates that the emission region is close to the compact object. Since the system's centre of mass is closer to the centre of mass of the star, the compact object appears to be orbiting the star. Hence, emission originating near the compact object would show a solid orbital modulation as the emission region moves toward and away from the observer. The sharp drop in emission after inferior conjunction approaching apastron, at this phase, is strongly dependent on the diminishing seed photon field in this region. At inferior conjunction, the emission is just below 5σ, then climbs to 7.8σ. The sharp rise may indicate that the peak may be further resolved in future studies.

5.7 Implications for gamma-ray emission

The observed gamma-ray emission is strongly modulated on the orbit, which is expected since the primary mechanism responsible for the emission is inverse Compton scattering, which depends on the energy density of the seed photon field and the angle at which the electron/positron scatters off the seed photon.

Naima Modelling

There needs to be more than the IC scattering model presented in this study to predict the TeV light curve.
LMC P3 has an eccentricity of ~ 0.4 (van Soelen et al. 2019), and LS 5039 is slightly less eccentric with $e \approx 0.35$ (Aragona et al. 2009), but LS 5039 has its GeV peak at superior conjunction (Abdo et al. 2009). LMC P3 peaks closer to the periastron passage, at a phase of $\sim$0.125 (Corbet et al. 2016). The orbital parameters found by van Soelen et al. (2019) puts periastron at $\sim$0.13. Abdalla et al. (2018) uses an electron spectrum with energies between 0.5 and 50 TeV and a total energy of 2.5×10^{38} erg to reproduce the flux given in the paper. The modelling done in this study set the total electron energy to 5×10^{37} erg to set the maximum spectral energy of the IC scattering curve shown in Figure 4.16 to be close to the observed flux maximum of $\frac{dN}{dE} = (3.1 \pm 0.5) \times 10^{-14}\text{cm}^{-2}\text{s}^{-1}\text{TeV}^{-1}$. The IC cooling time (Khangulyan et al. (2007), Eq. (1)) is of the order of hundreds of seconds, so with this cooling time and the total energy of the electrons, if the spin-down of a pulsar drives this system, the pulsar requires a spin-down energy of at least 10^{36}erg s^{-1}.
The observed gamma-ray emission is strongly modulated on the orbit. The inverse Compton light curve alone does not reproduce the emission peak in the correct position. This is because other physical processes are clearly at play (e.g. $\gamma\gamma$ absorption and Doppler boosting.)

Comparisons With other models

The VHE peak for LMC P3 has previously been found in the phase bin 0.2 -0.4 by the H.E.S.S. collaboration (Abdalla et al. 2018), and the result from this analysis places the peak of emission at 0.268-0.366. The phase shift between the *Fermi*-LAT GeV light curve and the TeV light curve can occur due to electron-positron pair production ($\gamma\gamma$ absorption), which becomes significant when the energy of the gamma-rays is greater than the rest mass of an electron. In the TeV range, this effect is very significant.
The competing processes of $\gamma\gamma$ absorption and IC scattering could peak around the superior conjunction, shifting the TeV maximum closer to the inferior conjunction, where the $\gamma\gamma$ opacity is the lowest. This, however, is assuming the inclination is 90°and a circular orbit.

The pair production threshold is given by,

$$\epsilon_\gamma \epsilon (1 - \cos\theta) \geq 2m_e^2 c^4$$

where ϵ_γ is the energy of a gamma-ray and ϵ is an optical stellar photon colliding at an angle θ in the stellar frame.
Considering a stellar photon with energy ϵ =1 eV, scattering at an angle of $\theta = 180°$,

$$\epsilon_\gamma (1 - \cos\theta) \geq \frac{2m_e^2 c^4}{\epsilon}$$

becomes

$$\epsilon_\gamma \geq \frac{2m_e^2 c^4}{2\epsilon}$$

which gives

$$\epsilon_\gamma \geq 240\text{GeV}$$

The Fermi-*LAT* energy range goes up to 300 GeV, which indicates that most of the absorption is more significant in the TeV energy range.
van Soelen et al. (2018) gives a model that shifts the peak closer to the observed phase of TeV emission. The model proposes a gamma-ray flux produced by IC scattering, absorbed by pair production, and mildly Doppler boosted ($\Gamma = 2$). The result is that the rise and fall time of the emission is much faster: the absorbed and boosted flux rises rapidly, approaching $\phi = 0.2$ and drops between $\phi \approx 0.35$ and 0.4. This effect will be faster for larger values of Γ.
Xingxing et al. (2020) presents a model where the density of the photon field modulates the IC flux, with Doppler boosting and pair production as well; however, their peak does not drop rapidly around the 0.2 to 0.4 phase range. This is explained in Xingxing et al. (2020) by the fact that they consider the travel distance, which makes the peak width wider.

5.8 Alternative solutions

The result from this study places the peak of emission after inferior conjunction. The orbital solution for LMC P3 given in van Soelen et al. (2019) does, however, have considerable uncertainty in the longitude of the periastron. The best fit for

the longitude of the periastron is $(11.3 \pm 12.0)^\circ$ (van Soelen et al. 2019). This uncertainty correlates to the uncertainties in the true anomaly bins. Considering this, the inferior conjunction occurs at 78.7°, so shifting this upward with the uncertainty of 12°gives 90.7°.

5.9 Limitations and Recommendations

The physical modelling was limited because only an inverse Compton model was studied. This model is also limited in assuming that the orbit has an inclination angle of $i = 90^\circ$. The inclination significantly impacts the shape of the peak: lower inclinations result in broader peaks, and higher inclinations tend to make the peak narrower since the emission region tends to sweep across our field of view; hence a sharper rise may indicate a high inclination. Multiple sources have already established (Abdalla et al. (2018); van Soelen et al. (2018); Xingxing et al. (2020)) that inverse Compton emission is not enough to explain the TeV emission for the system. More model components should be explored (e.g. $\gamma\gamma$ absorption, Doppler boosting, among others). The extreme rise and fall of significant emissions also indicate that the emission may be resolved further and can be undertaken in future studies.

Chapter 6

Conclusion

This study aimed to produce a data analysis of the gamma-ray binary, LMC P3. To this extent, a spectral analysis was conducted, and an orbitally resolved light curve was constructed. In addition, N 157B was used as a standard candle to ensure that the results for LMC P3 were credible.
This study aimed to investigate the orbitally variable TeV emission of LMC P3, using the orbital solution from van Soelen et al. (2019). The results indicate that the peak occurs after the inferior conjunction of the system. It was found that outside of this phase bin, the system does not have emission detectable by the HESS array. The physical model investigated included inverse Compton scattering, and it was found that this process alone is insufficient to imitate the observed gamma-ray modulation along the orbit.

6.1 Main Contributions

The phase of the emission peak was found to be at 0.268 - 0.366. This resolves the peak from 20% to 9.8%. With the current orbital parameters, this places the peak after the inferior conjunction. In addition, two additional flux points were produced, one before and one at inferior conjunction. This aims to create a light curve with three flux points and answers the research question of which orbital phase the emission occurs.

6.1.1 Implications

The peak occurring after inferior conjunction is unexpected since preliminary modelling with IC scattering, Doppler boosting, and $\gamma\gamma$ absorption predicts that the

peak would appear close to inferior conjunction (van Soelen et al. 2018). This means that extensive modelling is necessary or orbital solutions must be investigated. The narrowed peak can help tighten constraints on models and aid in testing a more comprehensive array of physical factors contributing to the modulation along the orbit.

6.2 Limitations

The HESS sensitivity limits prevent extensive probing of the VHE light curve. It is unlikely that using data from the HESS array alone, we will be able to see emissions from LMC P3 far into the off-peak regions. It may be possible to resolve the peak further and, with careful analysis, find emission before the peak phase bin. After the peak, this may be less likely since, at this point, the compact object is approaching apastron, so the seed photon field is significantly diminishing.
The time constraint limited the tested models: only an IC scattering model was produced, which was insufficient to make a comparable light curve.
This study did not investigate the disagreement in the spectrum of N 157B. The spectrum shows a higher flux, especially at lower energies and the reason behind this was not found. Future studies should investigate this disagreement which could result in a more consistent spectrum reproduction.

6.3 Recommendations

The ultimate goal of studying gamma-ray binary systems is to understand the physical processes in these systems. The main question of interest in this study has been *where* the TeV emission is coming from and *how* it evolves along the orbit of the system. These questions are an essential prerequisite which leads to the more significant questions of how the system produces gamma-rays, i.e. what physical processes are at play and to what extent? Can these systems significantly contribute to the cosmic ray spectrum we observe? The results presented in this work can help contribute to more constrained modelling, and a wider variety of models can be tested.

6.3.1 Further Research

There are many investigations which could not be answered in this work. However, there are indications that further resolution on the TeV peak could be undertaken. The result of the emission peak after inferior conjunction is inconclusive since different orbital solutions can be tested. These may yield inferior conjunction occurring later in orbit (where the rise of emission occurs), which would result in an agreement with predictions from previously established models. This system's energy-resolved spectral and timing studies can be undertaken to identify spectral energy shifts between energy ranges and energy-dependent light curves.
A more sensitive instrument, such as the CTA, can probe parts of orbit that fall below the HESS sensitivity, extending the light curve for LMC P3 and perhaps revealing finer details in the light curve.
A possible avenue to explore with the HESS data set that extends two decades is long-term variability studies. This can help test the accretion scenario, where outburst events are common (Naurois 2012).

Bibliography

Abdalla, H., Abramowski, A., Aharonian, F., et al. 2018, Astronomy & Astrophysics, 610, L17, publisher: EDP Sciences

Abdo, A., Ackermann, M., Ajello, M., et al. 2009, The Astrophysical Journal, 706, L56

Abramowski, A., Acero, F., Aharonian, F., et al. 2012, Astronomy & Astrophysics, 545, L2

Ackermann, M., Albert, A., Atwood, W. B., et al. 2016, Astronomy & Astrophysics, 586, A71, publisher: EDP Sciences

Aharonian, F., Akhperjanian, A., Aye, K.-M., et al. 2005a, Astronomy & astrophysics, 442, 1

Aharonian, F., Akhperjanian, A., Bazer-Bachi, A., et al. 2006a, Astronomy & Astrophysics, 457, 899

Aharonian, F., Akhperjanian, A. G., Aye, K. M., et al. 2005b, Science, 309, 746, aDS Bibcode: 2005Sci...309..746A

Aharonian, F., Akhperjanian, A. G., Bazer-Bachi, A. R., et al. 2006b, Astronomy & Astrophysics, 460, 743, number: 3 Publisher: EDP Sciences

Aharonian, F. A. 2004, Very High Energy Cosmic Gamma Radiation: A Crucial Window On The Extreme Universe (World Scientific), google-Books-ID: iALVC-gAAQBAJ

Aharonian, F. A. & Atoyan, A. M. 1981, Astrophysics and Space Science, 79, 321

Albert, J., Aliu, E., Anderhub, H., et al. 2006, science, 312, 1771

Aragona, C., McSwain, M. V., Grundstrom, E. D., et al. 2009, The Astrophysical Journal, 698, 514

Bamba, A., Ueno, M., Nakajima, H., Mori, K., & Koyama, K. 2006, Astronomy & Astrophysics, 450, 585, number: 2 Publisher: EDP Sciences

Berge, D., Funk, S., & Hinton, J. 2007, Astronomy & Astrophysics, 466, 1219, arXiv: astro-ph/0610959

Blumenthal, G. R. & Gould, R. J. 1970, Reviews of Modern Physics, 42, 237, publisher: American Physical Society

Bosch-Ramon, V. & Khangulyan, D. 2009, International Journal of Modern Physics D, 18, 347, aDS Bibcode: 2009IJMPD..18..347B

Bradt, H. 2008, Astrophysics processes: the physics of astronomical phenomena (Cambridge University Press)

Casares, J., Ribó, M., Ribas, I., et al. 2005, Monthly Notices of the Royal Astronomical Society, 364, 899

Chernyakova, M. & Malyshev, D. 2020, arXiv:2006.03615 [astro-ph], arXiv: 2006.03615

Chernyakova, M., Malyshev, D., Keague, S. M., et al. 2020, arXiv preprint arXiv:2005.14060

Cirkel-Bartelt, V. 2008, Living Reviews in Relativity, 11, 2

Collaboration, T. H. E. S. S. 2015, Science, 347, 406, publisher: American Association for the Advancement of Science Section: Report

Corbet, R. H. D., Chomiuk, L., Coe, M. J., et al. 2016, The Astrophysical Journal, 829, 105, publisher: American Astronomical Society

Czesla, S., Schröter, S., Schneider, C. P., et al. 2019, PyA: Python astronomy-related packages

De Naurois, M. & Rolland, L. 2009, Astroparticle Physics, 32, 231

Deil, C., Zanin, R., Lefaucheur, J., et al. 2017, in International Cosmic Ray Conference, Vol. 301, 35th International Cosmic Ray Conference (ICRC2017), 766

Dermer, C. D. & Giebels, B. 2016, Comptes Rendus Physique, 17, 594

Dubus, G. 2006a, Astronomy & Astrophysics, 451, 9, number: 1 Publisher: EDP Sciences

Dubus, G. 2006b, Astronomy & Astrophysics, 456, 801, number: 3 Publisher: EDP Sciences

Dubus, G. 2010, in High Energy Phenomena in Massive Stars, Vol. 422, 23

Dubus, G. 2013, The Astronomy and Astrophysics Review, 21, 64, publisher: Springer

Dubus, G. 2015, Comptes Rendus Physique, 16, 661

Gould, R. J. & Schréder, G. P. 1967, Physical Review, 155, 1404, publisher: American Physical Society

Greisen, E. W., Wells, D. C., & Harten, R. 1980, in Applications of Digital Image Processing to Astronomy, Vol. 264, International Society for Optics and Photonics, 298–300

Holler, M., Berge, D., Van Eldik, C., et al. 2015a, arXiv preprint arXiv:1509.02902

Holler, M., Berge, D., van Eldik, C., et al. 2015b, Observations of the Crab Nebula with H.E.S.S. Phase II, arXiv:1509.02902 [astro-ph]

Khangulyan, D., Aharonian, F., & Bosch-Ramon, V. 2007, Monthly Notices of the Royal Astronomical Society, 383, 467

Khangulyan, D., Aharonian, F. A., & Kelner, S. R. 2014, The Astrophysical Journal, 783, 100, publisher: American Astronomical Society

Kirk, J., Ball, L., & Skjæraasen, O. 1999, Astroparticle Physics, 10, 31

Kirk, J. G., Lyubarsky, Y., & Petri, J. 2009, in Neutron Stars and Pulsars, ed. W. Becker, Astrophysics and Space Science Library (Berlin, Heidelberg: Springer), 421–450

Komin, N., Haupt, M., & Collaboration, H. E. S. S. 2017, arXiv:1708.03171 [astro-ph], arXiv: 1708.03171

Komin, N., Haupt, M., & Collaboration, H. E. S. S. 2020, Search for Point-Like TeV Sources in the Large Magellanic Cloud, number: arXiv:1908.04656 arXiv:1908.04656 [astro-ph]

Longair, M. S. 2010, High energy astrophysics (Cambridge university press)

Martins, F., Schaerer, D., & Hillier, D. J. 2005, Astronomy & Astrophysics, 436, 1049, number: 3 Publisher: EDP Sciences

Mirabel, I. F. 2007, in The Multi-Messenger Approach to High-Energy Gamma-Ray Sources, ed. J. M. Paredes, O. Reimer, & D. F. Torres (Dordrecht: Springer Netherlands), 267–270

Naurois, M. d. 2012, Habiliation, Université Pierre et Marie Curie - Paris VI

of Encyclopaedia, T. E. 2013, True anomaly | astronomy | Britannica, https://www.britannica.com/science/true-anomaly, accessed: 2023-01-25

Paredes, J. M. & Bordas, P. 2019, Broad-band Emission from Gamma-ray Binaries, arXiv:1901.03624 [astro-ph]

Paredes, J. M., Martı, J., Ribó, M., & Massi, M. 2000, Science, 288, 2340

Pietrzyński, G., Graczyk, D., Gieren, W., et al. 2013, Nature, 495, 76

Rybicki, G. B. & Lightman, A. P. 1991, Radiative processes in astrophysics (John Wiley & Sons)

Seward, F. D., Charles, P. A., Foster, D. L., et al. 2012, The Astrophysical Journal, 759, 123, publisher: American Astronomical Society

Torres, D. F., Rea, N., Esposito, P., et al. 2011, The Astrophysical Journal, 744, 106

van Soelen, B., Komin, N., du Plooy, D., Väisänen, P., & Kniazev, A. 2018, in 63rd Annual Conference of the SA Institute of Physics (SAIP), 207–210

van Soelen, B., Komin, N., Kniazev, A., & Väisänen, P. 2019, Monthly Notices of the Royal Astronomical Society, 484, 4347

Weekes, T. C. 2003, Very high energy gamma-ray astronomy (CRC Press)

Wells, D. C. & Greisen, E. W. 1979, in Image processing in astronomy, 445

Weng, S.-S., Qian, L., Wang, B.-J., et al. 2022, Nature Astronomy, 6, 698, num Pages: 698-702 Place: London, United States Publisher: Nature Publishing Group

Xingxing, H., Jumpei, T., & Qingwen, T. 2020, Monthly Notices of the Royal Astronomical Society, 494, 3699, aDS Bibcode: 2020MNRAS.494.3699X

Zabalza, V. 2015, naima: a Python package for inference of relativistic particle energy distributions from observed nonthermal spectra, arXiv:1509.03319 [astro-ph]

Zabalza de Torres, V. 2011, accepted: 2013-04-23T13:18:38Z Publisher: Universitat de Barcelona